Shallow and Deep Convection Characteristics in the Greater Houston, Texas Area Using Cell Tracking Methodology

Kristofer S. Tuftedal[1], Bernat Puigdomènech Treserras[2], Mariko Oue[1], Pavlos Kollias[1,3]

[1]Division of Atmospheric Sciences, Stony Brook University, Stony Brook, NY, USA
[2]Department of Atmospheric and Oceanic Sciences, McGill University, Montréal, QC, Canada
[3]Center for Multiscale Applied Sensing, Brookhaven National Laboratory, Upton, NY, USA

Correspondence to: Kristofer S. Tuftedal *(kristofer.tuftedal@stonybrook.edu)*

Abstract. The convective lifecycle, from initiation to maturity and dissipation, is driven by a combination of kinematic, thermodynamic, microphysical, and radiative processes that are strongly coupled and variable in time and space. Radars have been traditionally used to provide the convective clouds characteristics. Here, we analyzed climatological convective cell radar characteristics to obtain and assess the diurnal cycle of shallow, modest deep, and vigorous deep convective cells that formed in the Greater Houston area, using the National Weather Service radar from Houston, Texas and a multi-cell identification and tracking algorithm. The examined dataset spans over four years (2018–2021) and for the warm season months (June to September). The analysis showed the clear diurnal cycles in cell initiation (CI), cell evolution parameters (e.g., maximum reflectivity, ~~cloud~~echo top height, and the height of maximum reflectivity), consistent with the sea breeze circulation. The cell evolution is well represented by relationships between 1) the height and value of the maximum radar reflectivity ~~and its height~~, 2) the ~~cloud~~echo top and the maximum vertically-integrated liquid, 3) the maximum reflectivity and columnar average reflectivity, and 4) ~~cloud~~echo top ascent rate and cell lifetime. The relationships presented herein help to identify the cell lifecycle stages such as early shallow convection, vigorous vertical development, anvil development, and convective core dissipation. ~~We also analyzed the near-storm environment to address any differences in the environmental conditions present at the time of CI and how they may differ between convective type (shallow, modest deep, and vigorous deep cells).~~

1 Introduction

Convection is one of the most important contributors to the Earth's climate system through its transport of heat, moisture, and momentum. These processes strongly depend on cloud evolution. While an ordinal convective cloud model is proposed, the cloud evolution may vary depending on environment, diurnal cycle, etc. (e.g. Bony et al. 2015; Fridland et al. 2017; Ladino et al. 2017; Colin and Sherwood 2021). These variabilities may cause large uncertainties in convective parameterizations in numerical climate and cloud models. Modeling studies have attempted to answer some of these outstanding questions (Lee et al. 2008; Zhu et al. 2012; Varble et al 2014; Igel et al. 2015; Peters et al. 2019), but the general lack of high-quality observational data to compare with these modelling studies makes it difficult to assess the validity of the results presented therein. Previous modeling studies tend to focus only on comparisons with observed reflectivity, which can be a rather convoluted to use for microphysical analyses. However, recent work in simulating polarimetric variables using forward operators (Ryzhkov et al. 2011; Wolfenberger and Bern 2018; Kumjian et al. 2019) may provide better insight into the changes in storm microphysics through comparisons with observed polarimetry.

The ongoing debate in the literature about warm- and cold-phase convective invigoration (i.e., Sheffield et al. 2015; Fan et al. 2018; Abbott and Cronin 2021; Igel and van den Heever 2021; Grabowski and Morrison 2021) is one such example of the need for high-quality observational datasets to compare with modeling studies. The collection of a robust observational dataset that can be used as observational benchmark for modeling studies is challenging. Such a dataset requires a sufficient large sample size of convective clouds properties over a wide range of meteorological and aerosol conditions and convective cell centric methodologies rather than domain averaging approaches that fail to capture the lifecycle of convective clouds.

To address some of the observational shortcomings and needs, a diverse, interagency, coordinated effort took place in the greater Houston, Texas metropolitan area and surrounding region from the summer of 2021 through the summer of 2022 to collect a comprehensive dataset of isolated convective cells (Jensen et al. 2022).These efforts include the Tracking Aerosol Convection interactions Experiment (TRACER) supported by the United States Department of Energy (DOE) Atmospheric Radiation Measurement (ARM) facility and the National Science Foundation (NSF) Experiment of Sea Breeze Convection, Aerosols, Precipitation and Environment (ESCAPE) campaign. The study region was selected because it is warm and humid in the summer and commonly experiences

Formatted: Indent: First line: 0.5"

onshore flow and sea breeze-forced convection. Recent studies on convective cells that form in coastal regions have illustrated that these cells are less influenced by the synoptic-scale meteorological conditions than cells that exist in only maritime or continental environments (e.g. Bergemann and Jakob 2016; Birch et al. 2016). The land-sea breeze circulation that develops in these regions ~~have~~has been shown to have a greater effect on local convection by acting as a forcing mechanism for convective initiation (CI) through an increase in surface convergence (Haurwitz 1947; Rotunno 1983). Study of convective cells that form under land-sea breeze circulation forced CI can be used to more directly attribute convective characteristics to ongoing convective processes rather than the synoptic-scale meteorological conditions present. This lack of dependence on the larger scale meteorology allows for more generalizable conclusions to be drawn for any convective characteristics presented herein.

Previous studies of long-term remote sensing data collected in Houston ~~suggests~~suggest that variability in convective cloud microstructure, hydrometeor properties, and electrification is correlated to variability in aerosol conditions over and downwind of Houston (Hu et al. 2019a, b). In these studies, NEXRAD radar observations were used to track convective cells during different cloud condensation nuclei (CCN) conditions (satellite-retrieved; Rosenfeld et al. 2016), and to investigate how variability in cloud, precipitation and lightning characteristics related to CCN conditions, though neglected proper control of meteorology. Also, a recent pilot study has identified the need to collect observations of convective clouds at a temporal and spatial resolution higher than is possible from the existing operational observations (Fridlind et al. 2019). Those studies show large variabilities of convective cloud properties associated with cloud lifecycles. In addition, cloud lifecycles also vary from one individual cloud to another. These substantial variabilities make it ~~difficult~~prudent to ~~understand general characteristics~~analyze very large datasets worth of ~~cloud lifecycle (evolution) by analyzing the lifecycles of a few~~ convective clouds to obtain more representative bulk statistics of these phenomena. This lack of generalizable data also hinders our ability to evaluate cloud model simulations.

Here, we add and expand on these previous studies using a similar methodology, but focusing on characteristics of both shallow and deep convection and utilizing an extensive convective-cell centric methodology for the different types of isolated convection observed around the Houston metropolitan and surrounding areas. The climatologies of the observed characteristics of shallow and deep convection are derived from the National Weather Service (NWS) KHGX Weather Surveillance Radar–1988 Doppler (WSR-88D; Crum 1993; Radar Operations Center

2022) and the Geostationary Operational Environmental Satellite-16 (GOES-16). ~~High Resolution Rapid Refresh model (HRRR; Smith et al. 2008; Dowell et al. 2022; James et al. 2022) data are also used to elucidate differences in the NSE between convective cell types.~~ Strict thresholding of the radar and satellite derived characteristics of tracked convective cells allows for the analysis of the behaviors of each case type (i.e., shallow, modest deep, and vigorous deep convection) distinct from one another. Sensitivity testing is also performed to determine how much the results presented herein vary with small variations in threshold selection. Section 2 outlines the data, threshold variables, and analysis methods used, section 3 presents the analyses of these convective types, and section 4 discusses the observations and results.

2 Data and Methods

2.1 Domain and Data

~~The area used for this~~Our study ~~was selected such that it~~domain was centered on the KHGX WSR-88D near Houston, Texas and extended ±125 km to the north, east, south, and west, creating a 250 km by 250 km domain. This region was selected because the coastline with the Gulf of Mexico generates regular land-sea breeze circulations which provide a forcing mechanism for CI. This domain also provides regions of relatively "pristine" and "polluted" aerosol regimes to the southwest and northeast respectively. The area to the northeast of Houston is generally downstream of pollution sources, such as the Houston metropolitan area itself and oil refineries near Houston allowing for the advection of this polluted air over this sub-region. The area to the southwest of Houston is generally upstream and made up of mostly rural land even further upstream, allowing the air here to be far less polluted.

Data from KHGX~~,~~ and GOES-16~~, and the HRRR~~ were collected for the period of June through September 2018–2021 where convective initiation occurred during local daytime (09:00–21:00 Central Daylight Time (CDT)). Initiation during local daytime was chosen to ~~ensure~~increase the likelihood that sea breeze propagation was a primary forcing mechanism for CI and to enable the analysis of GOES aerosol optical depth (AOD) data.

During the study period, the volume coverage patterns (VCPs) available to KHGX changed with the implementation of VCP 215 (15 elevation angles from 0.5 and 19.5°) and 112 (14 elevation angles from 0.5 and 19.5°) and the removal of VCPs 11, 211, 21, and 221 (Radar Operations Center 2015; Zittel 2019). Aside from these differing

VCPs, different dynamic scanning techniques can adjust how the radar scans without changing the VCP (Chrisman 2009; 2013; 2014; 2016). These differing VCPs and dynamic scanning techniques have an effect on the time required to complete a single VCP. Despite these variations in rescan time, the time required to complete any of these VCPs is on the order of approximately five minutes. These different VCPs also collect slightly different sets of elevation data, which can substantially affect the uncertainty in any height or vertically integrated liquid (VIL; Greene and Clark 1972; Amburn and Wolf 1997) analyses presented herein.

Horizontal radar reflectivity factor (Z_H) from KHGX was ~~gridded~~collected during normal weather surveillance operations and regridded to a 250 km by 250 km domain with 500 m by 500 m horizontal spacing for each ~~volume coverage pattern (VCP),~~case day considered, which was then used to estimate ~~vertically integrated liquid (VIL),~~VIL, radar-derived ~~cloud~~echo top height (~~CTH~~ETH), and radar-derived profile depth (H_{cell}). GOES-16 Channel 13 cloud top brightness temperature data (GOESBT) were analyzed such that each 5-minute image was linked to the KHGX scan time nearest to each GOESBT product time. GOES-16 AOD calculation requires cloud-free pixels to generate AOD data. In many cases, the location of cell initiation already contains some form of cloud cover (be it low-, middle-, or upper-level clouds) at the time of initiation, which inhibits AOD generation. When AOD values are generated, they are classified as low-, medium-, or high-quality returns. To ensure a large enough sample size, AOD data denoted as medium- or high-quality were temporally averaged for the 30 minutes preceding cell initiation at the location of cell initiation. ~~HRRR data were regridded to the same 500 m by 500 m grid used for Z_H.~~ We calculated ~~vertically integrated liquid (~~VIL~~)~~ from gridded Z_H data from KHGX using ~~the~~equation (1):

$$\sim\sim VIL\ (dB) = 10 * \log_{10}\left(\frac{\sum_{i=0}^{i=i_{max}} 3.44 * 10^{-6}[(Z_i + Z_{i+1})/2]^{4/7}dh}{1\ \sim\sim{}^{kg}/_{m^2}\sim\sim}\right)\sim\sim VIL\ (dB)$$

$$= 10 * \log_{10}\left(\frac{\sum_{i=0}^{i=(i_{max}-1)} 3.44 * 10^{-6}[(Z_i + Z_{i+1})/2]^{4/7}dh}{1\ {}^{kg}/_{m^2}}\right) \quad (1)$$

~~where Z is the radar reflectivity in units of $mm^6\ m^{-3}$.~~

where i_{max} is the total number of sweeps for a given VCP, Z is the radar reflectivity of a given sweep (i) in units of $mm^6\ m^{-3}$, and dh is the vertical spacing between sweeps. VIL assumes a Marshall-Palmer drop-size distribution, which

introduces uncertainty since this relationship may not be completely valid for convective events in coastal regions. Other sources of uncertainty in VIL include beam spreading with increasing distance from the radar and data sparsity at high elevations within 30 km of KHGX. The uncertainty because of beam spreading with distance has been shown to be relatively small, but that VIL within 30 km of the radar tends to be underestimated for 5-minute WSR-88D VCPs (Oue et al. 2022).

2.2 Cell Tracking

KHGX VIL and GOES-16 observations were used as input to a modified version of the multi-cell identification and tracking (MCIT) algorithm (Rosenfeld 1987; Gagin et al. 1985; Hu et al. 2019a) to track all features with VIL of ≥ -20 dB during that period. ~~The~~The specifics of the MCIT algorithm can be found in section 2.3 to 2.4.2 in Hu et al. 2019a and the modifications made to the ~~MCIT~~ algorithm are provided in detail in Lamer et al. (2023). The MCIT algorithm ingests time series of volume scans and tracks local maxima of VIL by identifying the two cells in consecutive radar scans that have common maximum VIL. (i.e. the areas of VIL have some overlap from one time to the next.) To check for overlap from timestep to the next, the pySTEPS (Pulkkinen et al. 2019a,b) is used to compute velocity fields to find the shift in images. The current image is then checked with the advected cell from the computed velocity field and checks for overlap between the actual cell and computed cell location. This tracking continues until the cell dies, splits, or merges. In addition to the ~~WSR-88D~~KHGX data, we used GOES-16 Channel 13 cloud top brightness temperature (GOESBT) to ~~isolate~~identify cold topped and warm topped cells. The initial analysis from the modified MCIT algorithm identified 1,664,215 features with a VIL value ≥ -20 dB during the analysis period.

2.3 Cell Classification

To better characterize evolution of each cell, we employed the following cloud properties:

1) ~~CTH~~ETH: the height at the middle of the highest gate with detectible signal (Z_H > -10 dBZ) from ~~the WSR-88D~~KHGX;
2) H_{cell}: the depth between the top of the highest gate of the radar detectible signal for a cell and the bottom of the lowest gate of the radar detectible signal. (not corrected for increasing altitude with increasing range from the radar).
3) ~~CRatio~~ERatio (Fig. 1): the ratio of the ~~CTH~~ETH to H_{cell}; and

Formatted: Subscript

Formatted: Subscript

4) the tracked cell area based on VIL (Area)

Using these properties, GOESBT, and VIL, we classified tracked features into three categories: 1) shallow, 2) modest deep, and 3) vigorous deep convective cells. Thresholds for the classification are listed in table 1. These thresholds were empirically derived to avoid false classification of cloud systems such as high cirrus clouds, mesoscale convective systems (MCSs), or large regions of stratiform precipitation. We also used the initial cluster fraction of the cell, which is the ~~ration~~ratio of the area of a given cell to the area of a cluster (parent) of the cell at the beginning of the cell lifetime, equal to 1 (a value of 1 meaning the cell is discrete). The split/merged cells are removed in this study~~.~~ using the process outlined in Lamer et al. (2023). The area threshold is used only to classify the shallow cells to ensure that these shallow features are not large regions of stratiform precipitation. This extensive thresholding removes noisy features, likely due to non-meteorological echoes (e.g., ground clutter, insects, etc.). Cells that have their "birth" or "death" occur on a domain edge are removed to avoid analyzing cases which are ongoing before or after entering or leaving the study domain. Cells which pass within 15 km of KHGX are also removed to mitigate the lack of data in the "cone of silence."

The shallow and deep convective cells selected based on these thresholds were then analyzed separately and compared with one another. Sensitivity studies were also performed on each case type by varying all thresholds (except initial cluster fraction and split/merge status) by ±5% individually and simultaneously to observe any changes in the distributions of certain variables for each case type (See Appendix).

2.4 Climatological Analyses and Statistical Analysis

Cell properties introduced in Sections 2.1 and 2.2 for all cells classified into the three categories during the four-year observation period were examined to allow for bulk analyses of cell type characteristics. Analyses used herein include observations during specific times during cells' lifetimes (such as the time of initiation), aggregates of all scans from the entire life of all cells of a given type, changes in variables over cell normalized lifetimes, diurnal changes in these variables, and spatial differences in initiation location. These analysis types enabled us to investigate how these cells changed as they grew, matured, and decayed, as well as allowed for the direct comparison of how these case types differ from each other.

To parse out any potential ~~environmental controls~~aerosol effects on shallow and deep CI and intensity~~,~~ ~~HRRR model data and~~ GOES-16 AOD data were analyzed. ~~The HRRR data were mined to collect the convective available potential energy (CAPE), convective inhibition (CIN), various shear parameters, and vertical profiles of temperature, dew point, and wind speed and direction interpolated to the grid point of a given cells' initiation point for the forecast hour prior to each cells' initiation time. The AOD data were analyzed to investigate any role that aerosol loading may play in affecting CI.~~ The nonparametric Mann-Whitney U test was used to investigate statistical differences between regional cell initiation AOD distributions (Mann and Whitney 1947). ~~To further elucidate any differences between case types or within a given case type, days where the number of cells of a specific type exceeded the 95th percentile of the number of cells for days where those cell types were present were selected and analyzed separately.~~

3 Results

3.1 Overall Cell Characteristics

The monthly average number of cells varies little from month to month for June, July, August, and September~~. All convective cell types have the~~, is highest ~~monthly average~~ in August ~~(Fig. 2). All three case types show little variability overall,~~ and has no significant difference ~~was found from month to month.~~

between months. The storm motion could be important to understand storm evolution. To evaluate the primary speed and direction of cell motion, figure 3 shows frequency distributions of the propagation speed and direction as a function of normalized lifetime for the three cell types investigated. The frequencies shown are normalized by the total number of samples at each normalized lifetime bin (every 0.025). All cell types tend to have storm motions ranging primarily ~~from the south~~between southerly to ~~east~~easterly. Shallow convective cells, overall, move the slowest out of the three cell types and have less variability in speed than modest and vigorous deep convective cell. Over the lifetime of these cells, shallow convective cell speed varies little and is much slower when compared to deep convection. ~~Both deep convective case types tend to accelerate with time with vigorous deep convective cells showing the most apparent tendency over their normalized lifetimes.~~ Overall, for the three categories, the convective cells mainly tend to have storm motions spanning from ~~southwest~~southwesterly to ~~east~~easterly. Larger variability in storm motion is found at the later period of the cell lifetime for modest and vigorous deep cells, where the greatest variability is seen in the vigorous deep cells. This finding suggests that some of the vigorous deep convective cells may be

Formatted: Indent: First line: 0"

supercellular in nature because of the large deviations from the early storm motions near the time of initiation, but cannot be confirmed without further analyses of detailed conditions for supercells outside of the scope of this research. The direction of motion of sea-breeze induced convective cells can depend on the low-level (i.e., 925 hPa) wind direction relative to the coastline (Die Wang, 2023, personal communication). The direction of cell motion (particularly early in the lifetimes of these cells) indicates the possibility that the sea breeze along the Gulf Coast plays a part in storm initiation and propagation as these directions would be consistent with the inland propagation of the sea-breeze, which propagates from southeast to northwest from the coastline.

3.2 Location and Diurnal Frequency of Initiation

Figure 4 shows the diurnal frequency of initiation times as a function of local time. All cell types have their peak in initiation in the late morning/early afternoon hours, which then sharply decreases as the day progresses. Overall, all types of convection in this region preferentially initiate in the late morning/early afternoon. However, there is a slight difference in peak time. Shallow convection and vigorous deep convection show earlier peaks in initiation time – between 10:00 and 14:00 CDT – when compared to the peak for modest deep convection, which is shifted slightly later (between 12:00 and 15:00; Fig. 4).

Figure 5 shows the initiation location for shallow (Fig. 5a,d,e), modest deep (Fig. 5b,e,h), and vigorous deep (Fig. 5c,f,i) convection. The three types all show a preference to initiate over land along the coastline to the southwest and northeast of Houston (within 100 km from the coast) with a local minimum in initiation over Galveston Bay, (the large bay to the east of Houston), suggesting that a land-sea contrast, hence sea breeze, is a key factor to initiate convection in this area. The inland propagation of the sea breeze can also be observed based on the cells' overall speed and direction of travel early in their lifetimes (Fig. 3). One feature of note is the obvious preference in shallow CI to the southwest of Houston (Fig. 5a,d,e). Another notable feature is that both moderate and vigorous deep convective cell types show a local maximum over the Houston metropolitan area, which is especially apparent in vigorous deep convective cases. This initiation maximum could be caused by the enhancement from aerosol loading and/or urban heating, but will need further examination in the future.

~~To further investigate if the sea breeze plays any potential roll in cell initiation, we divided initiation locations shown in figure 5 into four 3-hourly bins to analyze the spatial and diurnal variability in cell initiation (Fig. 6).~~ There is an obvious inland shift in initiation location, that is most obvious for vigorous deep convection, from the 09:00-

11:59 to 12:00-14:59 CDT period, further supporting the influence of the sea breeze on CI for all case types. The diurnal spatial shift in initiation location shows that the sea breeze is a key factor for CI along the coast. Figures 4 and 235 ~~6~~5 highlight that the early afternoon hours are the most preferable time for CI for all cell types. This is consistent with the previous studies (e.g., Park et al 2020).

The domain maximum in shallow CI to the southwest of Houston is also apparent in all periods except 18:00-20:59 CDT (not shown), but modest and vigorous deep convective types do not visually show the same southwest initiation preference. Rather, the two deep convective types (especially vigorous deep convection) do show maximums 240 in initiation over the Houston metropolitan area in the mid-to-late afternoon. We further speculate that this may be the result of urban heating allowing parcels to reach their convective temperatures during this time, even on days where CAPE is high, but CIN elsewhere in the domain is too strong to allow for other convection to initiate. However, as stated previously, further research is necessary to elucidate what mechanism(s) is(are) responsible for this local initiation maximum in deep convection.

245 **3.3 Diurnal Changes in Cell Characteristics**

To assess diurnal cycle of convective cells, we analyzed cell hour-by-hour basis characteristics for each scan for the duration of its life over the course of the day. Figure ~~7~~6 shows the diurnal trends in the distributions of GOESBT, the height of cell maximum radar reflectivity (H_{dBZmax}), and the cell maximum radar reflectivity (dBZ_{max}) for all scans of all convective cases. For shallow cells, the GOESBT tends to be constant at around 285 K over time, 250 and the majority of the cells have H_{dBZmax} ~~below 5 km, suggesting warm precipitation processes.~~ In contrast, the two deep convection types exhibit similar maximum frequencies of GOESBT before noon with a substantial shift of the maximum frequency to ~240 K for modest deep cells and ~220 K for the vigorous deep cells around noon, then taper off into the later evening and overnight hours. The frequency peak of H_{dBZmax} for the modest and vigorous convective types is found below 6 km before noon, similar to shallow cells, which then shifts to 6–10 km for modest deep cells 255 and 9–13 km for the vigorous deep cells until ~18:00 CDT for modest deep cells and 23:00 CDT for vigorous deep cells. ~~The rapid change in GOESBT and HdBZmax shows the quick vertical evolution of these cells resulting in cold precipitation processes. CTH~~ETH also shows the same change in characteristics as GOESBT and H_{dBZmax} (not shown), further supporting late morning/early afternoon initiation. There is little dependency of maximum reflectivity on time.

3.4 Analysis of Bulk Cell Type and Normalized Cell Lifetime Characteristics

Even though the peak in CI has been shown to occur in the late morning/early afternoon, and peak in intensity in the early-to-mid afternoon, there may be diurnal variability and differences in duration in cell lifetime that are unaccounted for. To observe how these cells behave over the course of their respective lifetimes rather than the course of a given day, we have analyzed these cells by aggregating scans during specific periods of cell lifetimes, aggregating all scans of all cells of each type, and by normalizing each by its respective lifetime. These analyses allow for direct comparisons of case types, regardless of what time the cells initiated or how long they lasted.

The growth and decay of these cells can be seen by analyzing the change in the distributions of dBZ_{max}, H_{dBZmax}, maximum VIL, GOESBT, and the average of the maximum radar reflectivity for all columns within a given cell (dBZ_{avg}). Shallow convective cells show overall low dBZ_{max} at low H_{dBZmax} over the course of entire cell lifetimes (Fig. ~~8~~7). Cell growth and decay is apparent, as H_{dBZmax} and dBZmax shift to overall higher values during the first half of cell lifetimes and then decrease back to a distribution that looks most similar to cell initiation at the end of their lives. Modest and vigorous deep convection show clear signals of the birth (Fig. ~~8b~~7b,c), mature (Fig. ~~8e~~7e,f,h,i), and dissipation (Fig. ~~8k~~7k,l) phases. Early in their lifetimes, these cell types are dominated by low dBZ_{max} values at low H_{dBZmax}, which both increase considerably moving into their mature phases. This trend is especially apparent in vigorous deep convection, where early in cell lifetimes, there is a clear signal of initiation and some cells that have begun to grow (based on the secondary maximum in high dBZ_{max} at high H_{dBZmax} values). As these cells continue to mature, we see that H_{dBZmax} remains high, but that dBZ_{max} begins to decrease. This is indicative of cells where the convective core has dissipated leaving "orphan anvils" (Hitschfeld 1960). However, H_{dBZmax} appears to be slightly skewed by bright banding, as both modest and vigorous deep convection show rather unnatural looking discontinuities in their distributions around 6 km above radar level ~~(ARL)~~. These discontinuity features are especially apparent in figure 8b,e.

Formatted: Subscript

Figure ~~9~~8 supports that the feature seen in figure ~~8~~7 around 6 km ~~ARL~~above radar level to be caused by the bright band, since there are no similar discontinuities in these distributions where GOESBT is warmer. ~~As with figure 8, figure 9~~However, this is one interpretation and the discontinuities shown in figure 7 may rather be indicative of some ongoing storm physics. As with figure 7, figure 8 clearly shows the initiation, growth, and decay of these cell types. Shallow convective cells remain at relatively warm GOESBT and low maximum VIL throughout their lives, whereas modest and vigorous deep convection show clear growth from warm GOESBT, low maximum VIL cells to cold GOESBT high maximum VIL cells. ~~Also shown as in figure 8~~The rapid changes shown in figures 7 and 8 during

the early stages of vigorous deep convective shows the quick vertical evolution of these cells. Also shown as in figure 7, is the dissipation phase, where GOESBT remains cold, but VIL drops off considerably. This further supports the idea that this is the period when the convective cores have dissipated, leaving orphan anvils behind.

As stated previously, dBZ_{avg} is the average of the column Z_H maximums within a given cell and dBZ_{max} is the cell maximum Z_H for a given time. To investigate potential anvil generation, the distributions of dBZ_{avg} versus dBZ_{max} are analyzed (Fig. ~~10).~~9). During the anvil generation phase, we would expect cells to be at their most intense state, meaning they would have a high value of dBZ_{max}. We would also expect an increasingly large region of low Z_H high aloft in the storm to form. This region of low Z_H will skew dBZ_{avg} lower while dBZ_{max} will remain unaffected until the storm begins to dissipate. When comparing shallow and deep convection with this information in mind, the feature, apparent in deep convection, of low dBZ_{avg} and high dBZ_{max} ~~is indicative of~~could be interpreted as anvil generation. As with previous figures in this section, these anvil signatures are especially apparent in vigorous deep convective cells. Early in deep convective lifetimes, cells have not had enough time to grow to a state where anvil generation is possible (with the exception of the most intense cells). The vast majority of cells exist very near the one-to-one line of dBZ_{avg} to dBZ_{max} with only a small subset of cells moving into the high dBZ_{max} and lower dBZ_{avg} indicative of cells growing and beginning to produce anvils (Fig. ~~10c~~9c). As cells move into the mature portion of their lives, the low dBZ_{avg}/high dBZ_{max} region, where strong, anvil generating cells are present, becomes the dominant regime for these cells (Fig. ~~10f~~9f,i). As cells decay, the distribution maximum shifts back down near the one-to-one line (Fig. ~~10l~~9l), which would be suggestive of orphan anvils, given the analyses provided in the previous paragraphs. One feature of note in the vigorous deep convective cells during the dissipation phase is the secondary maximum in the high dBZ_{avg}/high dBZ_{max}. ~~We suspect that this is not a physical process and rather an artifact of cells leaving our tracking domain prior to reaching dissipation.~~This feature represents the transition from the mature stage having the large dBZ_{max} in a deeper depth within the clouds to the later stage having lower dBZ_{max} during the normalized lifetime 0.75 – 1.0.

~~The full lifetime distributions of dBZmax, HdBZmax, maximum VIL, GOESBT, and dBZavg can be seen in figures 11 and 12. These plots show the full aggregation of scans considered in figures 8, 9, and 10 and further highlight how these cell types change over their lives. The majority of the shallow convective cells remain relatively warm-topped with low water contents, whereas deep convective cells begin in a similar parameter space as shallow convection and grow into cold-topped, high water content cells. The maximum in HdBZmax that we suspect is caused~~

Formatted: Subscript

Formatted: Subscript

Formatted: Subscript

Formatted: Subscript

~~by bright banding is also clearly apparent. Based on Theil-Sen Estimator regressions performed on the GOESBT versus maximum CTH for all three case types, 6 km ARL would be approximately equivalent to a GOESBT of 260 K (Fig. 13). Theil-Sen Estimator regression was used to mitigate the effects on the maximum CTH distribution from convective cells where their maximum CTHs are artificially skewed downward when within the cone of silence for KHGX. While there is a secondary maximum in GOESBT at around 260 K for modest deep convection, the same maximum does not appear in vigorous deep convection, further suggesting that these maximums in HdBZmax are at least partially caused by bright banding.~~

Shallow convective cells reach their maximum ~~CTH~~ETH during approximately the first 10% of their life, appear to maintain this height until around 75%, and then gradually decrease in height until dissipation (Fig. ~~14a~~10a). Modest convective cells take substantially longer (~35-55% of the way through their life) to reach their maximum ~~CTH~~ETH and then sharply decrease in height during the last 15% (Fig. ~~14b~~10b). Vigorous convective cells, on the contrary, reach their maximum ~~CTH~~ETH quite quickly (within the first 15 to 35% of their life), maintain a tall ~~cloud~~echo top, and then gradually decrease in height to dissipation (Fig. ~~14c~~10c). The gradual decrease in ~~CTH~~ETH leading to dissipation is further indicative of convective anvils. In this case, we believe this signal further supports that we are observing convective core dissipation, thus leaving orphan anvils behind. Both H_{dBZmax} and dBZ_{max} show similar trends to ~~CTH~~ETH for all case types. Shallow convective cells reach their dBZ_{max} and H_{dBZmax} early in the cells' normalized lifetime (within the first 20-30%), maintain, and then gradually decay to dissipation (Fig. ~~14d~~10d,g). Modest convection shows a gradual increase in H_{dBZmax} that looks nearly identical to its maximum ~~CTH~~ETH. It appears that these cells reach their H_{dBZmax} anywhere from 35 to 65% of the way through their lifetimes. However, dBZ_{max} is reached much earlier (within the first 20% of their life) than H_{dBZmax} (Fig. ~~14e~~10e,h). Vigorous deep convection reaches its H_{dBZmax} much sooner in its normalized lifetime (between 10 and 25% of their normalized lives), like ~~CTH~~ETH (Fig. ~~14f~~10f). As with modest deep convection, vigorous deep convection also reaches its dBZ_{max} early in its life (within the first 20% of their normalized life) and maintains these values until about halfway through their lives, when dissipation begins (Fig. ~~14i~~10i). One feature that is seen in dBZ_{max} and H_{dBZmax} for both modest and vigorous deep convection is the apparent bimodality at the ~~end~~later of these cells' lifetimes~~,~~ (>~0.4), where it appears that some cells maintain high values of dBZ_{max} and VIL (not shown) at the higher altitudes (~9 km) all the way up to dissipation (Fig. ~~14f~~10f,i)~~.~~ ~~We suspect that this~~This is ~~not a physical difference between~~particularly apparent in the modest deep cells. This bimodality suggests that some ~~cells and others and is rather caused by some~~of the modest

Formatted: Default Paragraph Font

deep cells ~~leaving our observation domain while still in their mature stage instead of dissipating within the domain~~with lower ETHs were dominated by warm phase precipitation processes similar to the shallow cells, as H_{dBZmax} was found below 6 km through the lifetime. This reasoning would explain why dBZ_{max} and VIL remain so high all the way up to the end of their life, as they are deemed "dissipated" when leaving the domain, even though these cells may still persist for some time.

Cell echo base height (H_{EBase}) was determined using the maximum ~~CTH~~ETH minus the radar-derived echo profile depth to estimate the precipitation base of these cells. For shallow convection, H_{EBase} remains relatively flat for the duration of these cells, ~~but~~whereas it shows an increase in height during dissipation for modest and vigorous deep convective cells (Fig. ~~14~~j10j,k,l). This signature is especially apparent in the vigorous deep convective cells. This increase in H_{EBase}, in tandem with the minimal decrease in maximum ~~CTH~~ETH during dissipation of both types of deep convection (especially vigorous deep convection), reinforces the idea that we are observing the generation of orphan anvils. The bimodality here may also partially be caused by some cells leaving the domain during their mature phase, prior to dissipation despite the mitigation techniques we applied, but this is less certain than for the reasoning given for dBZ_{max}.

In an attempt to quantify vertical motion within ~~these~~vigorous deep convective cells, we approximated this quantity three different ways. We used the maximum ~~CTH~~ETH, and H_{dBZmax} during each scan, and GOESBT at the time closest to radar scan time with the time between samples to calculate maximum ~~CTH~~ETH and H_{dBZmax} "ascent rates," as well as GOESBT "cloud top lapse rates." As shown in figure ~~15~~11, there are ~~clear~~ maximum ~~CTH~~ETH and H_{dBZmax} ascent signatures early and descent signatures late in the lives of these cells for all case types. GOESBT shows cooling during the same period where ascent is seen and warming during the same period where descent is seen in maximum ~~CTH~~ETH and H_{dBZmax}. The near identical timing and structure of these derived ascent rates suggest that these values may be good proxies for updraft intensity during the early parts of these cell. However, the later portions of these cells' lives are dominated by the tops or high upper portions of these features (as shown in figure ~~14~~11) and most likely do not represent downdraft intensity during dissipation. We suspect that, in vigorous deep convective cases, we may be seeing orphan anvils falling out as virga since the descent signature occurs quite late in these cells' normalized lifetimes after their H_{EBase} increases considerably. Maximum ~~CTH~~ETH and H_{dBZmax} descent rates and GOESBT warming rates match well late in these cells' lives, which further supports the idea that we may be observing

Formatted: Subscript
Formatted: Subscript
Formatted: Subscript
Formatted: Subscript
Formatted: Subscript
Formatted: Subscript
Formatted: Subscript
Formatted: Subscript

anvil fall-out. Further analysis is necessary to validate these results. There is a hint of this signature as well for modest deep convective cells, but it is not as obvious. To further assess the quality of these approximations, analyses outside the scope of this study will be needed. One caveat to consider with these ascent rate results is the increasing uncertainty in ETH and H_{dBZmax} with increasing range from KHGX. This uncertainty may account for the large spread always shown since we have large sample sizes for all case types. The large uncertainty for cells in the farthest portions of our domain muddle these results considerably. However, since the same signal is seen when looking at the GOESBT cloud top lapse rates, more credence is led to the above analyses.

~~**3.5 Near Storm Environment Analyses**~~

~~To elucidate any effects from the local meteorology where these cells formed, HRRR data for the hour directly preceding cell initiation are extracted for the grid point where initiation occurs. The surface-based environment does not appear to play a role in differentiating whether cells become shallow or deep convective cells. All convective types initiated in environments where surface-based CAPE and CIN are similar overall. Storm relative helicity (SRH) and bulk shear are also similar overall. Deep convective cases formed in environments with slightly higher 0-1 km SRH, but the distributions of 0-1 km and 0-3 km SRH, as well as 0-6 km bulk shear are similar (not shown).~~

~~When observing the composite soundings for the initiation locations for all convective case types, the temperature profiles and parcel paths are also nearly identical. Dew point, however, is drier in the mid-to-upper levels for the initiation locations of shallow convective cells when compared to deep convective cells (Fig. 16). While there is substantial spread in the moisture profile in all case types, modest and vigorous deep convection moisture profiles appear essentially the same. The wind profiles also appear relatively similar between case types. Surface winds are slightly backed and veer with height to about 850 hPa, where they begin to back again (especially in shallow convective cases.) However, the magnitude of these differences in mean wind are quite small (on the order of 5 kts between 850 hPa and 600 hPa.) There are also apparent differences in upper-level winds, but again, are quite small in magnitude.~~

In order to further parse out any differences in initiation environment, we select case days where the number of cells that initiated on a given day, for a given case type, surpassed the 95th percentile of daily cell initiation (273, 61, and 43 cells for shallow, modest deep, and vigorous deep convective cells respectively). The composite soundings for the initiation locations of the cell type that surpassed the 95th percentile of daily cell counts are shown in figure 17. As with the soundings from figure 16, the key difference between these case types is that shallow convective initiation locations tend to have drier mid-to-upper-level dew points. Near surface winds are nearly the same with some apparent differences in mid and upper-level winds.

Previously, we noted the discrepancy in initiation location of shallow convective cells that did not appear to be affecting deep convection. There is either some form of enhancement occurring to the southwest of the Houston metropolitan area or some form of suppression occurring to the northeast. One potential cause for this discrepancy could be the local meteorology in which these cells form. On days where shallow convective cells surpassed the 95th percentile of daily shallow convective cell initiations, we subdivided the domain to isolate the region to the southwest and northeast of Houston (Fig. 18a,b). The composite soundings for shallow convective cell initiation locations within these sub-domains are shown in figures 18c and 18d. While the moisture profile to the southwest of Houston is marginally drier in the mid-to-upper levels, these soundings are essentially identical. One interpretation of these results is that drier air aloft tends to inhibit convective updrafts from growing into deep convection. The entrainment of this drier air aloft would cause more evaporative cooling at the cloud top than a moister environment, leading to more negative buoyancy, and therefore limiting updraft intensity.

To compare with modest and vigorous deep convection, we computed the total number of cells that formed within each sub-domain and for both sub-domains combined, then normalized them by the area of each domain. For shallow convection, the southwest domain had a cell initiation of 0.2074 cells km-2, the northeast domain had a cell initiation of 0.1764 cells km-2, and the combined southwest and northeast domain showed a total of 0.1920 cells km-2. Modest deep convective cells had a cell initiation of 0.0389 cells km-2 to the southwest, 0.0358 cells km-2 to the northeast, and 0.0373 cells km-2 combined. Vigorous deep convective cells had a cell initiation of 0.0331 cells km-2 to the southwest, 0.0265 cells km-2 to the northeast, and 0.0298 cells km-2 combined. Overall, more cells initiated in the southwest area than the northeast area. These area-normalized initiation counts show that there may be some slight differences in deep CI between the areas to the southwest and northeast of Houston. These results combined with the

~~near identical soundings for shallow convection suggest that something other than local meteorology is affecting shallow CI.~~

3.5 Aerosol Effect Analysis

One potential ingredient that may influence CI and has been a key point of debate in recent literature is aerosol loading. ~~We~~Aerosol particles in this region range from natural particles, such as sea spray, to industrial pollutants from oil refineries and urban sources. However, no such dataset exists which is tracks individual aerosol species on the spatiotemporal scale needed for direct comparison with MCIT output. As such, we used temporal averages of GOES-16 AOD at the locations of cell initiation for the 30 minutes prior to MCIT detected initiation. We analyzed these data for regions to the southwest and northeast ~~sub-domains shown in Fig. 18a,b, but performed the analysis over the entire 4-year climatological dataset, rather than the subsets~~ of ~~days discussed in the preceding paragraphs.~~Houston. The analyses of AOD for shallow and modest deep (Fig. ~~19a~~12a,b) cells at the locations of their initiation show essentially identical distributions from southwest to northeast; the primary difference being that both shallow and modest deep cells exhibit a longer tail toward higher AOD values to the southwest. Median (mean) AOD for shallow convective cell initiation locations were 0.~~340~~338 (0.400) to the southwest and 0.335 (0.366) to the northeast, and 0.366 (0.~~448~~453) to the southwest and 0.~~340~~346 (0.~~379~~384) to the northeast for modest deep convection. Considering the substantial difference in initiation location for shallow convection and nearly identical initiation AOD distributions, this result can be interpreted that bulk AOD does not play an important role in controlling cell initiation. However, this does not mean that aerosol particles play no role as a control on cell initiation. Rather, it may be specific species of aerosol particles that are more or less important to these processes. Vigorous deep convective cells, however, do show differing distributions from southwest to northeast (Fig. 19c). As with shallow and modest deep convection, vigorous deep convection also exhibits a longer tail extending to higher values of AOD to the southwest. The initiation locations for vigorous deep convective cells tend to have marginally higher AOD values to the southwest. The median (mean) of the AOD distributions for vigorous deep convective cell initiation locations was 0.~~433~~428 (0.513) to the southwest and 0.~~366~~373 (0.~~383~~396) to the northeast. However, these differences in distributions are not statistically significant. From the previous area-normalized cell initiation, we speculate that the marginally higher values of AOD and rates of cell initiation to the southwest in vigorous deep convection suggest that aerosol loading may indeed factor into vigorous deep CI, but that more marginal convective cells are either more

dependent on specific species of aerosol particles rather than overall aerosol loading or are not as affected by aerosol loading overall.

4 Summary and Discussion

The climatological characteristics of convective cell evolution and their diurnal cycles were analyzed using the ~~National Weather Service (~~NWS~~)~~ ~~Weather Surveillance Radar – 1988 Doppler (~~ KHGX WSR-88D~~)~~ from Houston, Texas ~~(KHGX)~~ for the warm season months (June to September) from 2018 and 2021 and a modified version of the ~~multi-cell identification and tracking (~~MCIT~~)~~ algorithm. In total, this study analyzed ~~52,216~~48,800 convective cells (~~38,465~~35,995 shallow cells for ~~151,995~~142,923 volume scans, ~~8,514~~7,935 modest deep cells for ~~101,845~~92,798 volume scans, and ~~5,237~~4,869 vigorous deep cells for ~~105,666~~95,219 volume scans). Analysis of these case types together allowed for the direct comparison of cell characteristics and the environments in which they form. The key findings from this study are:

1. CI for all cell types occurs most frequently in the late morning/early afternoon over land, consistent with the inland incursion of the sea breeze front.
2. There is a spatial variability in CI for shallow, modest, and vigorous deep convective cells, suggesting some effects of aerosol loading and/or urban heating. This is particularly clear for shallow cells. ~~Surface conditions do not appear to have any obvious effect on the resulting cell types that form in a given location. They exhibit slightly higher AOD values~~Higher AOD values tend to be present to the southwest of Houston, which is most easily observed when looking at the vigorous deep CI AOD distributions. While these results are not statistically significant, they suggest that aerosol loading may have some effect on deep CI. The initiation biases do not appear to be related to overall aerosol loading based on the pre-CI AOD analysis with the exception of vigorous deep cells. Further analysis using high spatiotemporal aerosol and urban heat data will be needed.
3. ~~The CI location bias for shallow cells was coincident with slightly drier mid-to-upper-level moisture to the southwest of Houston, based on the HRRR reanalysis data. The deep convection categories do not appear to be related to the local meteorology at the point of initiation based on the HRRR reanalysis data. The surface-based CAPE and CIN do not show significant relations with CI.~~

4.3. The modest and vigorous deep convective cells particularly deepen in the afternoon/evening (12:00-21:00 CDT) as the frequency peak of their heights of maximum reflectivity increase to 11 km and that of the brightness temperature decrease to 220 K. The shallow cells do not have clear diurnal variability in those parameters.

5.4. The cell evolution is well represented by relationships between the following cell properties:

1) The height and value of the maximum radar reflectivity ~~and its height~~: The developing stage (cell lifetime normalized by cell duration < 0.75) is well represented by an exponential curve as the H_{dBZmax} gradually increases from around 2 to 4 km with a maximum reflectivity of ~50 dBZ, which then dramatically increases to a height of 12 km for dBZ_{max} values of 50-60 dBZ. These coincident increases in dBZ_{max} and H_{dBZmax} occur in the early stage of cell lifetime (normalized lifetime < 0.5). The dissipation stage is represented by a wide distribution of the maximum reflectivity at a high altitude (~10 km) suggesting anvil development and convective core dissipation.

2) The brightness temperature (hence ~~cloud~~echo top height) and the maximum VIL: The developing stage (normalized lifetime < 0.75) is well represented by an exponential curve as the brightness temperature gradually decreases from 290 to 260 K from the maximum VIL until 10 dB then dramatically decreases to 210 K for VIL > 10 dB.

3) The maximum reflectivity and columnar average reflectivity: As the cells begin to develop for all case types, these variables remain near the one-to-one line. However, as deep convective cells (especially vigorous deep convective cells) reach the middle phases of their lifecycles (0.25 < normalized lifetime ≤ 0.75), an obvious extension of high dBZ_{max}/low dBZ_{avg} becomes apparent. The extension of the distribution during this period further supports the development of anvils. In the remaining 25% of vigorous deep convective cell lifetimes, the distribution of dBZ_{max}/dBZ_{avg} shifts to low values for both, suggesting convective core dissipation leaving only orphan anvils behind.

6.5. The ~~CTH~~ETH ascent rate is slightly more positive (0.3 km/min) in the early stage (normalized lifetime < 0.4) and negative for the later stage (normalized lifetime > 0.8) for deep convective cells. Early in these cells' lives, the cell tops grow vertically as they intensify and the rates at which they ascent should be close to the actual updraft intensity. Late in the cells' lives, H_{dBZmax} remains high aloft as it appears that H_{dBZmax} remains

in the anvil portion of the storm after it reaches maturity. These descent rates are likely to be representative of orphan anvils falling out as virga.

Based on the findings in this study, the analysis techniques presented can identify individual features within convective cells. Further parsing of these data may allow for the tracking of individual features within cells, such as tracking cores and anvils separately and being able to analyze their behaviors over their lives. Polarimetric variables can also be added, as in Hu et al. (2019a,b), for automated tracking of features such as differential reflectivity columns and arcs. The convective cells considered in this study only constitute about 3% of the features tracked during the climatology period and were selected based on the empirically derived thresholds in table 1. Some of the features we excluded by using these thresholds are non-meteorological in nature, but others include high clouds and large precipitation shields. Different empirically derived thresholds can be developed to isolate these and other features from the full dataset and used to create large climatologies of these features of interest. The analysis techniques presented in this study can also be applied to the cloud resolving model simulations using radar simulator and cell tracking techniques (e.g. Oue et al. 2022). ~~This~~Analyses of this type will aid in better ~~evaluate the~~evaluating simulation results to understand isolated convective cell formation and evolution mechanisms including effects of environmental factors such as aerosols. Some such formation mechanisms have been discussed here, such as aerosol loading and urban heating, but have not been explored in-depth, but may be of considerable importance in determining what processes are most important to convective growth, maintenance, and decay.

Appendix

To assess the sensitivity of the results in this study, the thresholds were varied individually and simultaneously by ±5% from the values presented in table 1. The number of cells selected in each sensitivity test were recorded and plots were qualitatively analyzed to investigate substantial visual differences as these variables were adjusted. Table A1 shows the number of cells selected for each variable adjusted. Figure A1 shows the visual differences of the distributions based on changes in the most sensitive thresholds.

The number of shallow convective cases varied more for lifetime minimum GOESBT than any other variable. The number of cases increased by 16.~~94~~79% for a five percent reduction in the GOESBT threshold (from 268.0 K to

254.6 K) and decreased by 48.~~99~~97% for a five percent increase in the same threshold (from 268.0 K to 281.4 K). The visual differences in the distributions of cases are shown in figure A1a,b,c. As shown, the visual differences in the distributions are caused by the addition or removal of colder topped shallow convection (Fig. A1c). The overall shape of the distribution does not change otherwise. Increasing GOESBT only removes the more "intense" shallow convective cells that have colder GOESBT values during their lifetimes.

Like the shallow convective cases, the number of modest deep convection cases varied most with changes in lifetime minimum GOESBT. There was a 27.~~01~~23% reduction in cases with a five percent decrease in GOESBT (250.0 K to 237.5 K). This removes the slightly warmer GOESBT cloud tops, leaving an upper bound of more intense modest deep convective cases (Fig. A1e). There was also a ~~23.94~~24.40% increase in cases with a five percent increase in lifetime minimum GOESBT (250.0 K to 262.5 K). This clearly shows the addition of warmer, lower intensity convective cells (Fig. A1f). The modest convective cells also varied by more than 10% for the upper bound of the lifetime maximum ~~CTH~~ETH, but there were no visible changes in distributions of these variable, only a reduction/increase in the number of cases (Fig. A1g,h,i).

Vigorous convection varied most by lifetime maximum ~~CTH~~ETH. The number of cases increased by 28.~~36~~94% for a five percent decrease in maximum ~~CTH~~ETH (12 km to 11.4 km) and decreased by 26.~~79~~95% for a five percent increase in maximum ~~CTH~~ETH (12 km to 12.6 km). The variability in maximum ~~CTH~~ETH is shown in figure A1j,k,l and appears to behave similarly to how the sensitivity in maximum ~~CTH~~ETH affects modest deep convection. Adjusting this threshold, only appears to reduce or increase the number of cases and not change the shape of the distribution.

Author Contribution

Kristofer S. Tuftedal performed the threshold selection processes, all analyses presented herein, and the bulk of manuscript preparation. Bernat Puigdomènech Treserras wrote the script for the MCIT algorithm and generated the dataset analyzed in this paper. Mariko Oue provided assistance in the interpretation of results and assistance in preparing this manuscript. Pavlos Kollias provided assistance in the interpretation of results, suggestions for analysis techniques, and assistance as a Ph.D. advisor to Kristofer S. Tuftedal.

Code Availability

The MCIT tracking algorithm and analysis codes are available upon request.

Data Availability

The datasets generated for this study are available upon request. All other datasets used (WSR-88D KHGX~~,~~ and GOES-16~~, and HRRR~~) in this study are freely available through the National Centers for Environmental Information.

Competing Interests

The authors declare that they have no conflict of interest.

Acknowledgements

This study was supported by NSF Grant AGS-2019968 (Kollias and Oue) and the U.S. Department of Energy DE-SC0021160 (Oue). The authors would like to thank the three anonymous reviewers whose comments helped improve the content and clarity of this manuscript.

References

Amburn, S. A., and P. L. Wolf, 1997: VIL Density as a hail indicator. *Wea. Forecasting*, **12**, 473–478, doi:10.1175/1520-0434(1997)012<0473:VDAAHI>2.0.CO;2.

Bergemann, M., and C. Jakob, 2016: How important is tropospheric humidity for coastal rainfall in the tropics? *Geophys. Res. Lett.*, **43**, 5860–5868, doi:10.1002/2016GL069255.

Formatted: Font: Italic

Formatted: Font: Not Bold

Birch, C. E., S. Webster, S. C. Peatman, D. J. Parker, A. J. Matthews, Y. Li, and M. E. E. Hassim, 2016: Scale interactions between the MJO and the western maritime continent. *J. Climate*, **29**, 2471–2492, doi:10.1175/JCLI-D-15-0557.1.

Bony, S., B. Stevens, D. M. W. Frierson, C. Jakob, M. Kageyama, R. Pincus, T. G. Shepherd, S. C. Sherwood, A. P. Siebesma, A. H. Sobel, M. Watanabe, and M. J. Webb, 2015: Clouds, circulation, and climate sensitivity. *Nature Geoscience*, **8**, 261–268, doi:10.1038/ngeo2398.

Chrisman, J. N., 2009: Automated Volume Scan Evaluation and Termination (AVSET)—A simple technique to achieve faster volume scan updates. 34th Conf. on Radar Meteorology, Williamsburg, VA, Amer. Meteor. Soc., P4.4, https://ams.confex.com/ams/34Radar/techprogram/paper_155324.htm.

Chrisman, J. N., 2013: Dynamic scanning. NEXRAD Now, 22, 1–3, https://www.roc.noaa.gov/WSR88D/PublicDocs/NNOW/NNow22c.pdf.

Chrisman, J. N., 2014: Multiple elevation scan option for SAILS (MESO-SAILS)—The next step in dynamic scanning for the WSR-88D. Radar Operations Center, 27 pp., https://www.roc.noaa.gov/wsr88d/PublicDocs/NewTechnology/MESO-SAILS_Description_Briefing_Jan_2014.pdf.

Chrisman, J. N., 2016: Mid-volume rescan of low-level elevations (MRLE): A new approach to enhance sampling of quasi-linear convective systems (QLCSs). New Radar Technologies Web Page, NOAA/NWS/Radar Operations Center, 21 pp., https://www.roc.noaa.gov/WSR88D/PublicDocs/NewTechnology/DQ_QLCS_MRLE_June_2016.pdf.

Colin, M., and S. C. Sherwood, 2021: Atmospheric convection as an unstable predator-pray process with memory. *J. Atmos. Sci.*, **78**, 3781–3797, doi:10.1175/JAS-D-20-0337.1.

~~Dowell, D. C.,~~Crum, T. D. and R. L. Alberty, 1993: The WSR-88D and the WSR-88D operational support facility. *Bull. Amer. Meteor. Soc.*, **74**, 1669–1688, doi: 10.1175/1520-0477(1993)074<1669:TWATWO>2.0.CO;2.

~~C.~~ R. Alexander, E. P. James, S. S. Weygandt, ~~S.~~ G. Benjamin, G. S. Manikin, B. T. Blake, J. M. Brown, J. B. Olson, M. Hu, T. G. Smirnova, T. Ladwig, J. S. Kenyon, R. Ahmadov, ~~D.~~ D. Turner, J. D. Duda, and T. I. Alcott, 2022: The High-Resolution Rapid Refresh (HRRR): An hourly updating convection-allowing forecast model. Part I: Motivation and system description. ~~*Wea.*~~ Forecasting, 37, 1371–1395, doi:10.1175/WAF-D-21-0151.1.

Fan, J., D. Rosenfeld, Y. Zhang, S. E. Giangrande, Z. Li, L. A. T. Machado, S. T. Martin, Y. Yang, J. Wang, P. Artaxo, H. M. J. Barbosa, R. C. Braga, J. M. Comstock, Z. Feng, W. Gao, H. B. Gomes, F. Mei, C. Pöhlker, U. Pöschl, and R. A. F. De Souza, 2018: Substantial convection and precipitation enhancements by ultrafine aerosol particles. *Sci.*, **359**, 411–418, doi:10.1126/science.aan8461.

Fridlind, A. M., X. Li, D. Wu, M. van Lier-Walqui, A. S. Ackerman, W. Tao, G. M. McFarquhar, W. Wu, X. Dong, J. Wang, A. Ryzhkov, P. Zhang, M. R. Poellot, A. Neumann, and J. M. Tomlinson, 2017: Derivation of aerosol profiles for MC3E convection studies and use in simulations of the 20 May squall line case. *Atmos. Chem. Phys.*, **17**, 5947–5972, doi:10.5194/acp-17-5947-2017.

Fridlind, A. M., M. van Lier-Walqui, S. Collis, S. E. Giangrande, R. C. Jackson, X. Li, T. Matsui, R. Orville, M. H. Picel, D. Rosenfeld, A. Ryzhkov, R. Weitz, and P. Zhang, 2019: Use of polarimetric radar measurements to constrain simulated convective cell evolution: a pilot study with Lagrangian tracking. *Atmos. Meas. Tech.*, **12**, 2979–3000, doi:10.5194/amt-12-2979-2019.

Formatted: Font: Italic

Gagin, A., D. Rosenfeld and R. E. Lopez, 1985: The relationship between height and precipitation characteristics of summertime convective cells in south Florida. *J. Atmos. Sci.*, **42**, 84–94.

Grabowski, W. W., and H. Morrison, 2021: Supersaturation, buoyancy, and deep convection dynamics. *Atmos. Chem. Phys.*, **21**, 13997–14018, doi:10.5194/acp-21-13997-2021.

Greene, D. R., and R. A. Clark, 1972: Vertically Integrated Liquid Water – A new analysis tool. *Mon. Wea. Rev.*, **100**, 548–552, doi:10.1175/1520-0493(1972)100<0548:VILWNA>2.3.CO;2.

Haurwitz, B., 1947: Comments on the sea-breeze circulation. *J. Atmos. Sci.*, **4**, 1–8, doi:10.1175/1520-0469(1947)004<0001:COTSBC>2.0.CO;2.

Hitschfeld, W., 1960: The motion and erosion of convective storms in severe vertical wind shear. *J. Atmos. Sci.*, **17**, 270–282, doi:10.1175/1520-0469(1960)017<0270:TMAEOC>2.0.CO;2.

Hu, J., D. Rosenfeld, D. Zrnic, E. Williams, P. Zhang, J. C. Snyder, A. Ryzhkov, E. Hashimshoni, R. Zhang, and R. Weitz, 2019a: Tracking and characterization of convective cells through their maturation into stratiform storm elements using polarimetric radar and lightning detection. *J. Atmos. Res.*, **226**, 192–207, doi:10.1016/j.atmosres.2019.04.015.

Hu, J., D. Rosenfeld, A. Ryzhkov, D. Zrnic, E. Williams, P. Zhang, J. C. Snyder, R. Zhang, and R. Weitz, 2019b: Polarimetric radar convective cell tracking reveals large sensitivity to cloud precipitation and electrification properties of CCN. *J. Geophys. Res. Atmos.*, **124**, 12194–12205, doi:10.1029/2019jd030857.

Formatted: Font: Italic

Formatted: Font: Italic

Igel, A. L., M. R. Igel, and S. C. van den Heever, 2015: Make it a double? Sobering results from simulations using single-moment microphysics schemes. *J. Atmos. Sci.*, **72**, 910–925, doi:10.1175/JAS-D-14-0107.1.

Igel, A. L., and S. C. van den Heever, 2021: Invigoration or enervation of convective clouds by aerosols? *Geophys. Res. Lett.*, **48**, e2021GL093804, doi:10.1029/2021GL093804.

James, E. P., C. R. Alexander, D. C. Dowell, S. S. Weygandt, S. G. Benjamin, G. S. Manikin, J. M. Brown, J. B. Olson, M. Hu, T. G. Smirnova, T. Ladwig, J. S. Kenyon, and D. D. Turner, 2022: The High-Resolution Rapid Refresh (HRRR): An hourly updating convection-allowing forecast model. Part II: Forecast performance. *Wea.* Forecasting, 37, 1397–1417, doi:10.1175/WAF-D-21-0130.1.

Jensen, M. P., J. H. Flynn, L. M. Judd, P. Kollias, C. Kuang, G. Mcfarquhar, R. Nadkarni, H. Powers, and J. Sullivan, 2022: A succession of cloud, precipitation, aerosol, and air quality field experiments in the coastal urban environment. *Bull. Amer. Meteor. Soc.*, **103**, 103–105, doi:10.1175/BAMS-D-21-0104.1.

Kumjian, M. R., C. P. Martinkus, O. P. Prat, S. Collis, M. van Lier-Walqui, and H. C. Morrison, 2019: A moment-based polarimetric radar forward operator for rain microphysics. *J. Appl. Meteor. Climatol.*, **58**, 113–130, doi:10.1175/JAMC-D-18-0121.1.

Ladino, L. A., A. Korolev, I. Heckman, M. Wolde, A. M. Fridlind, and A. S. Ackerman, 2017: On the role of ice-nucleating aerosol in the formation of ice particles in tropical mesoscale convective systems. *Geophys. Res. Lett.*, **44**, 1574–1582, doi:10.1002/2016GL072455.

Formatted: Font: Italic

Formatted: Font: Italic

Formatted: Font: Italic

Formatted: Font: Italic

Lamer, K., P. Kollias, E. P. Luke, B. P. Treserras, M. Oue, B. Dolan, 2023: Multisensor agile adaptive sampling (MAAS): a methodology to collect radar observations of convective cell life cycle. *J. Atmos. Oceanic Technol.*, submitted.

Lee, M., S. D. Schubert, M. J. Suarez, J. E. Schemm, H. Pan, J. Han, and S. Yoo, 2008: Role of convection triggers in the simulations of the diurnal cycle of precipitation over the United States Great Plains in a general circulation model. *J. Geophys. Res. Atmos.*, **113**, D02111, doi:10.1029/2007JD008984.

Mann, H. B., and D. R. Whitney, 1947: On a test of whether one of two random variables is stochastically larger than the other. *Ann. Math. Stat.*, **18**, 50–60, doi:10.1214/aoms/1177730491.

Oue, M., S. M. Saleeby, P. J. Marinescu, P. Kollias, and S. C. van den Heever, 2022: Optimizing radar scan strategies for tracking isolated deep convection using observing system simulation experiments. *Atmos. Meas. Tech.*, **15**, 4931–4950, doi:10.5194/amt-15-4931-2022.

Park, J. M., S. C. van den Heever, A. L. Igel, L. D. Grant, J. S. Johnson, S. M. Saleeby, S. D. Miller, and J. S. Reid, 2020: Environmental controls on tropical sea breeze convection and resulting aerosol redistribution. *J. Geophys. Res. Atmos.*, **125**, e2019JD031699, doi:10.1029/ 2019JD031699.

Peters, K., C. Hohenegger, and D. Klocke, 2019: Different representation of mesoscale convective systems in convection-permitting and convection-parameterizing NWP models and its implications for large-scale forecast evolution. *Atmos.*, **10**, 503, doi:10.3390/atmos10090503.

Pulkkinen, S., D. Nerini, A. Perez Hortal, C. Velasco-Forero, U. Germann, A. Seed, and L. Foresti, 2019: Pysteps: an open-source Python library for probabilistic precipitation nowcasting (v1.0). *Geosci. Model Dev.*, **12**, 4185–4219. doi:10.5194/gmd-12-4185-2019.

Pulkkinen, S., D. Nerini, A. Perez Hortal, C. Velasco-Forero, U. Germann, A. Seed, and L. Foresti, 2019: pysteps - a community-driven open-source library for precipitation nowcasting. *Poster presented at the 3rd European Nowcasting Conference*, Madrid, ES. doi: 10.13140/RG.2.2.31368.67840.

Radar Operations Center, 2015: WSR-88D Volume Coverage Pattern (VCP) improvement initiatives. New Radar Technologies Web Page, NOAA/NWS/Radar Operations Center, 8pp., https://www.roc.noaa.gov/WSR88D/PublicDocs/NewTechnology/New_VCP_Paradigm_Public_Oct_2015.pdf.

Radar Operations Center, 2022: NEXRAD technical information. NEXRAD Technical Information Web Page, NOAA/NWS/Radar Operations Center, https://www.roc.noaa.gov/WSR88D/Engineering/NEXRADTechInfo.aspx.

Rosenfeld, D., 1987: Objective method for analysis and tracking of convective cells as seen by radar. *J. Atmos. Oceanic Technol.*, **4**, 422–434.

Rosenfeld, D., Y. Zheng, E. Hashimshoni, M. L. Pöhlker, A. Jefferson, C. Pöhlker, X. Yu, Y. Zhu, G. Liu, Z. Yue, B. Fischman, Z. Li, D. Giguzin, T. Goren, P. Artaxo, H. M. J. Barbosa, U. Pöschl, and M. O. Andreae, 2016: Satellite retrieval of cloud condensation nuclei concentrations by using clouds as CCN chambers. *Proc. Natl. Acad. Sci. USA*, **113**, 5828–5834, doi:10.1073/pnas.1514044113.

Formatted: Font: Italic

Rotunno, R., 1983: On the linear theory of the land and sea breeze. *J. Atmos. Sci.*, **40**, 1999–2009, doi:10.1175/1520-0469(1983)040<1999:OTLTOT>2.0.CO;2.

Ryzhkov, A., M. Pinsky, A. Pokrovsky, and A. Khain, 2011: Polarimetric Radar Observation Operator for a Cloud Model with Spectral Microphysics. *J. Appl. Meteor. Climatol.*, **50**, 873–894, doi:10.1175/2010JAMC2363.1.

Sheffield, A. M., S. M. Saleeby, and S. C. van den Heever, 2015: Aerosol-induced mechanisms for cumulus congestus growth. *J. Geophys. Res. Atmos.*, **120**, 8941–8952, doi:10.1002/2015JD023743.

~~Smith, T. C., S. G. Benjamin, *J.* M. Brown, S. Weygandt, T. Smirnova, and B. Schwartz, 2008: Convective forecasts from the hourly updated, 3-km high resolution rapid refresh (HRRR) model. 24th Conf. on Severe Local Storms, Savannah, GA, Amer. Meteor. Soc., 11.1, https://ams.confex.com/ams/24SLS/techprogram/paper_142055.htm.~~

Varble, A., E. J. Zipser, A. M. Fridlind, P. Zhu, A. S. Ackerman, J. Chaboureau, S. Collis, J. Fan, A. Hill, and B. Shipway, 2014: Evaluation of cloud-resolving and limited area model intercomparison simulations using TWP-ICE observations: 1. Deep convective updraft properties. *J. Geophys. Res. Atmos.*, **119**, 13891–13918, doi:10.1002/2013JD021371.

Wolfensberger, D. and A. Berne, 2018.: From model to radar variables: a new forward polarimetric radar operator for COSMO, *Atmos. Meas. Tech.*, **11**, 3883–3916, doi:10.5194/amt-11-3883-2018.

Formatted: Font: Italic

Zhu, P., J. Dudhia, P. R. Field, K. Wapler, A. Fridlind, A. Varble, E. Zipser, J. Petch, M. Chen, and Z. Zhu, 2012: A limited area model (LAM) intercomparison study of a TWP-ICE active monsoon mesoscale convective event. *J. Geophys. Res. Atmos.*, **117**, D11208, doi:10.1029/2011JD016447.

Zittel, W. D., 2019: Theory and concept of operations for multi-PRF dealiasing algorithm's VCP 112. New Radar Technologies Web Page, NOAA/NWS/Radar Operations Center, 13 pp., https://www.roc.noaa.gov/WSR88D/PublicDocs/NewTechnology/Theory_ConOps_VCP112.pdf.

Tables

	Shallow Convection	Modest Deep Conv.	Vigorous Deep Conv.
Initial Cluster Fraction	1	1	1
Lifetime Min. GOESBT	≥ 268 K	≤ 250 K	≤ 250 K
Lifetime Max. VIL	≥ -10 dB	≥ 0 dB	≥ 0 dB
Lifetime Max. ~~CTH~~ETH	< 8 km	8 ≤ ~~CTH~~ETH < 12 km	≥ 12 km
Lifetime Max. ~~CRatio~~ERatio	≥ 0.60	≥ 0.75	≥ 0.75
Lifetime Max. Area	≤ 30 km^2	N/A	N/A
Splits/Merges Removed	Yes	Yes	Yes
# of cells	~~3846~~35996	~~8514~~7935	~~5237~~4869
# of radar scans	~~151995~~142923	~~10184~~92798	~~10566~~95219

Table 1: A table of the thresholds used to isolate shallow, modest deep, and vigorous deep convection from all tracked features from the modified version of the MCIT algorithm.

Figures

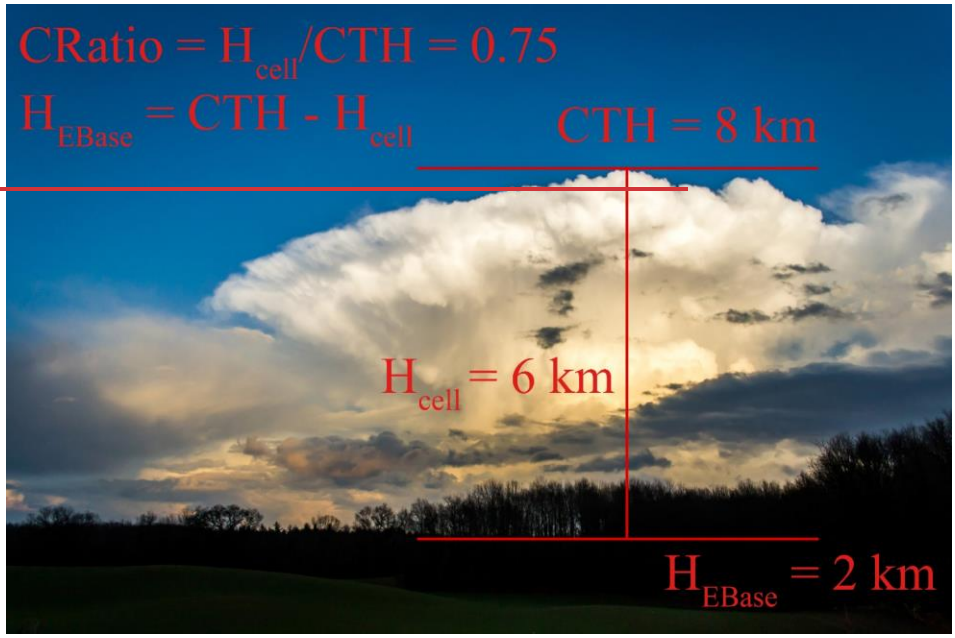
CRatio = H_{cell}/CTH = 0.75
H_{EBase} = CTH - H_{cell}
CTH = 8 km
H_{cell} = 6 km
H_{EBase} = 2 km

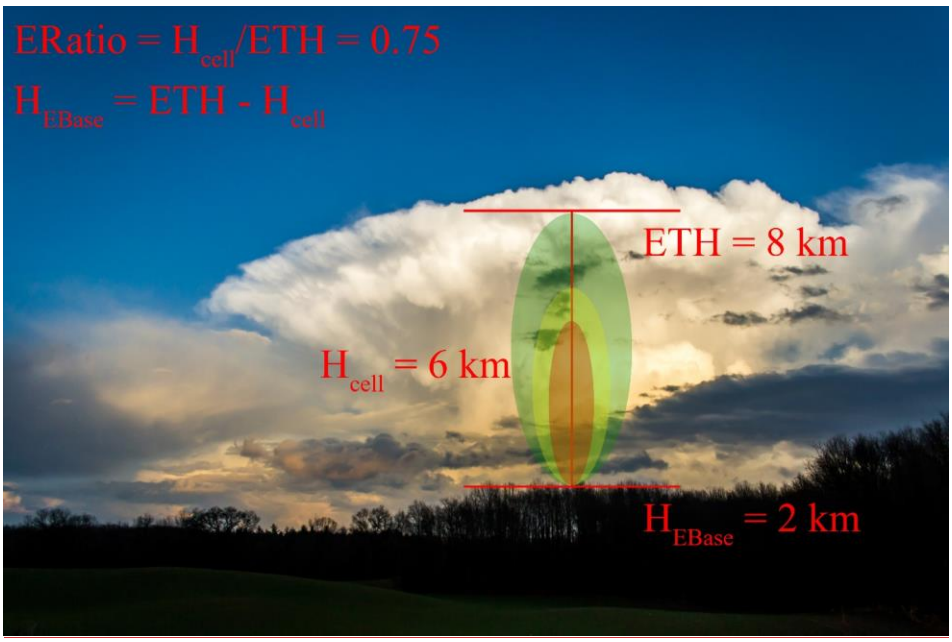

Figure 1: A visual illustration of ~~CRatio~~ERatio, H_{cell}, and H_{EBase}. This image is meant to provide a visual context for these three variables. The ~~actual values of CRatio~~red, yellow, and green shaded areas represent arbitrary high, medium, and low reflectivity contours respectively. ERatio and H_{EBase} are calculated using the maximum ~~CTH~~ETH and H_{cell}, which are radar-derived quantities and will always be less than the actual height of the storm top and physical depth of a given cell.

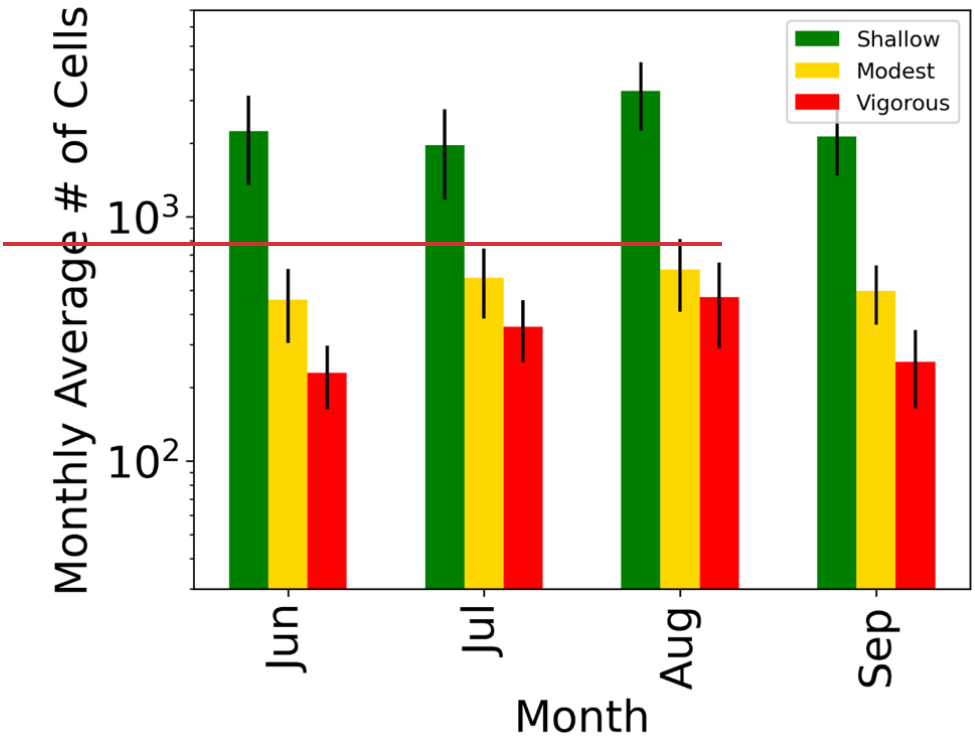
Shallow
Modest
Vigorous
Monthly Average # of Cells
10^3
10^2
Jun
Jul
Aug
Sep
Month

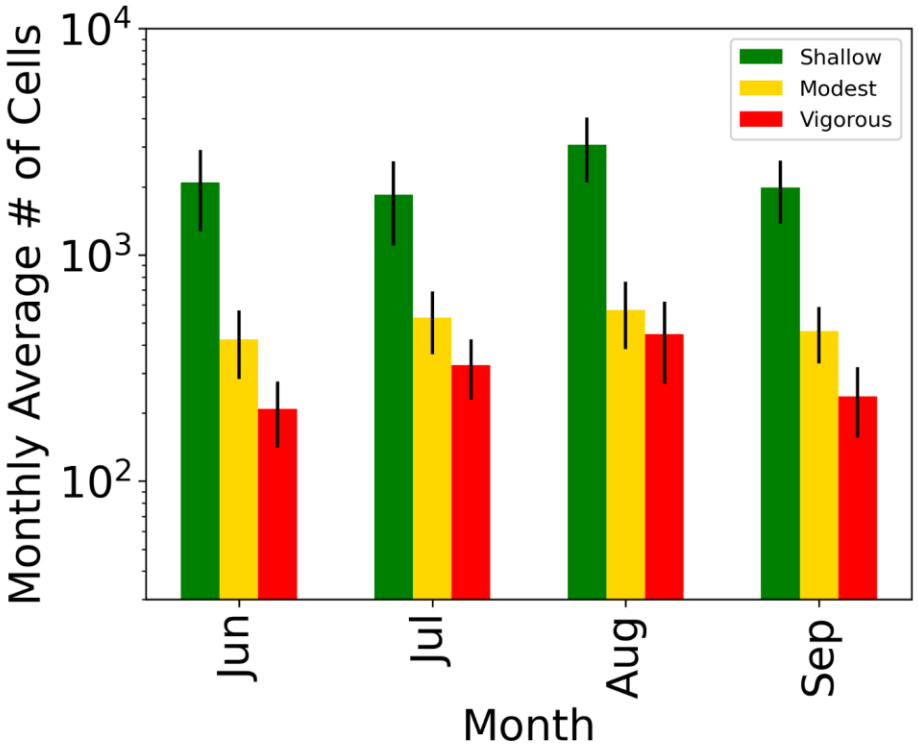

Figure 2: Bar graphs showing the monthly average cell count for shallow (green), modest deep (yellow), and vigorous deep (red) convection. The vertical black lines at the top of each bar denote ± one standard deviation.

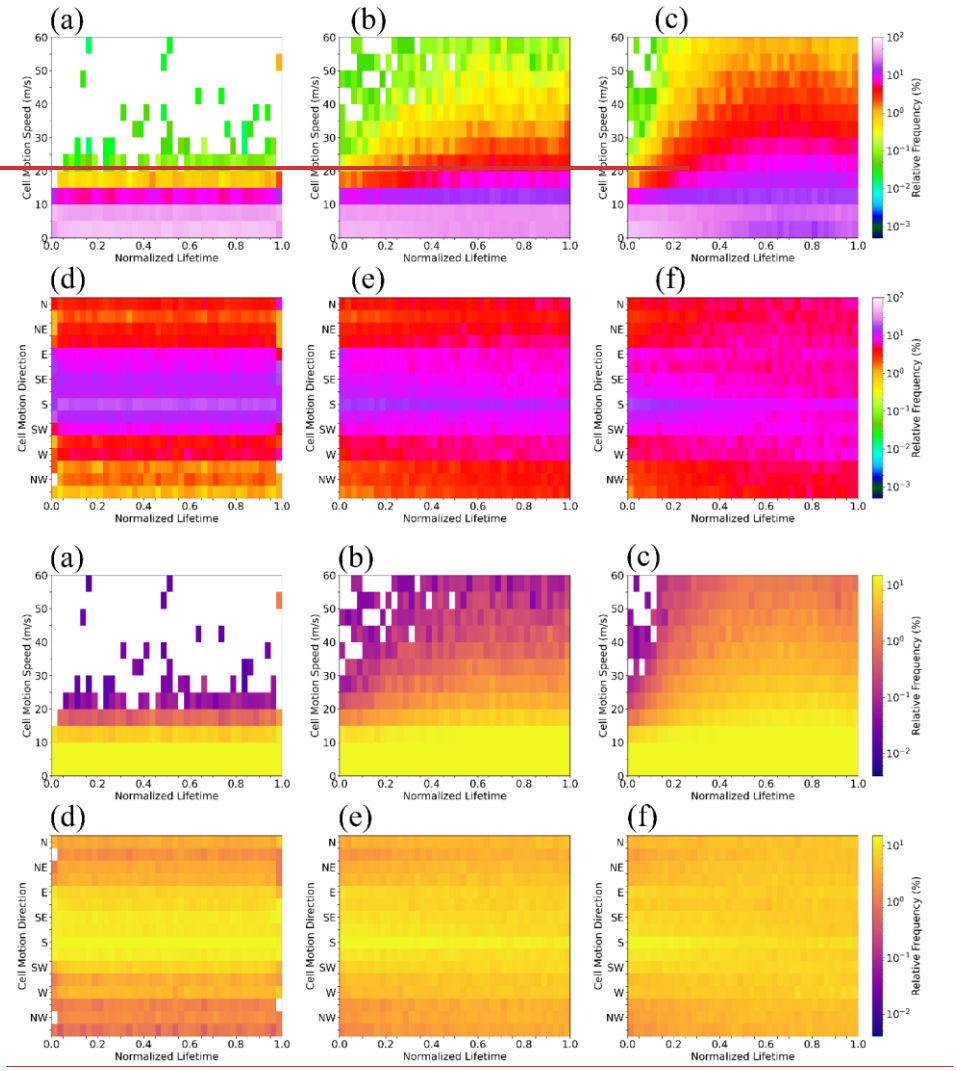

Figure 3: The normalized lifetime distributions of the bin count normalized cell motion speed (a, b, c) and cell motion direction (d, e, f) for all shallow (a, d), modest deep (b, e), and vigorous deep (c, f) convective cells.

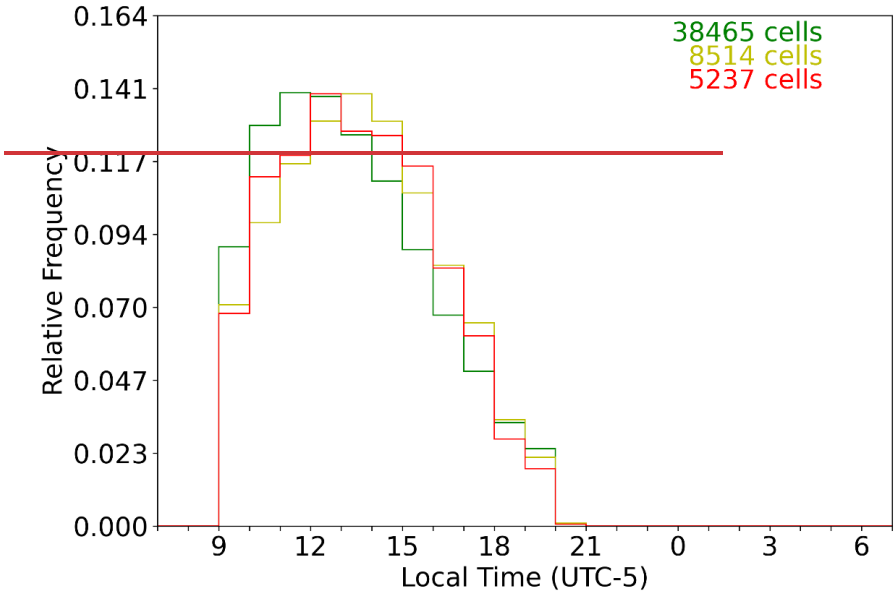
38465 cells
8514 cells
5237 cells
Relative Frequency
0.164
0.141
0.117
0.094
0.070
0.047
0.023
0.000
9
12
15
18
21
0
3
6
Local Time (UTC-5)

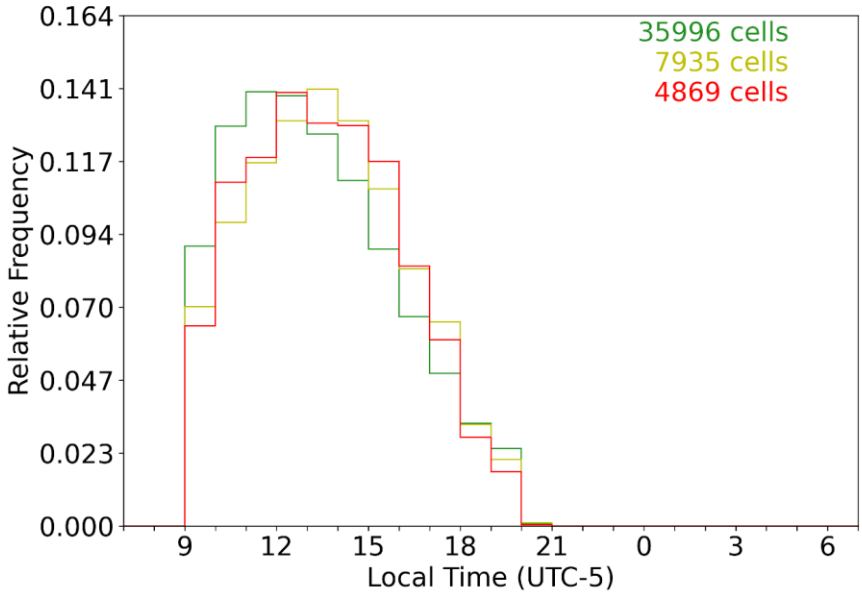

Figure 4: The frequency of initiation based on local time of day for (green) shallow convection, (yellow) modest deep convection, and (red) vigorous deep convection.

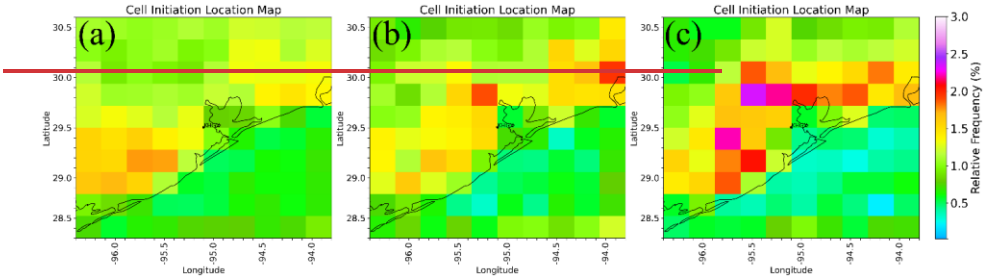

780 ~~Figure 5: Maps showing the spatial distributions of initiation locations normalized by the total number of cells of each type for (a) shallow, (b) modest deep, and (c) vigorous deep convection. The black dot in each denotes the location of the KHGX WSR-88D radar used in this study.~~

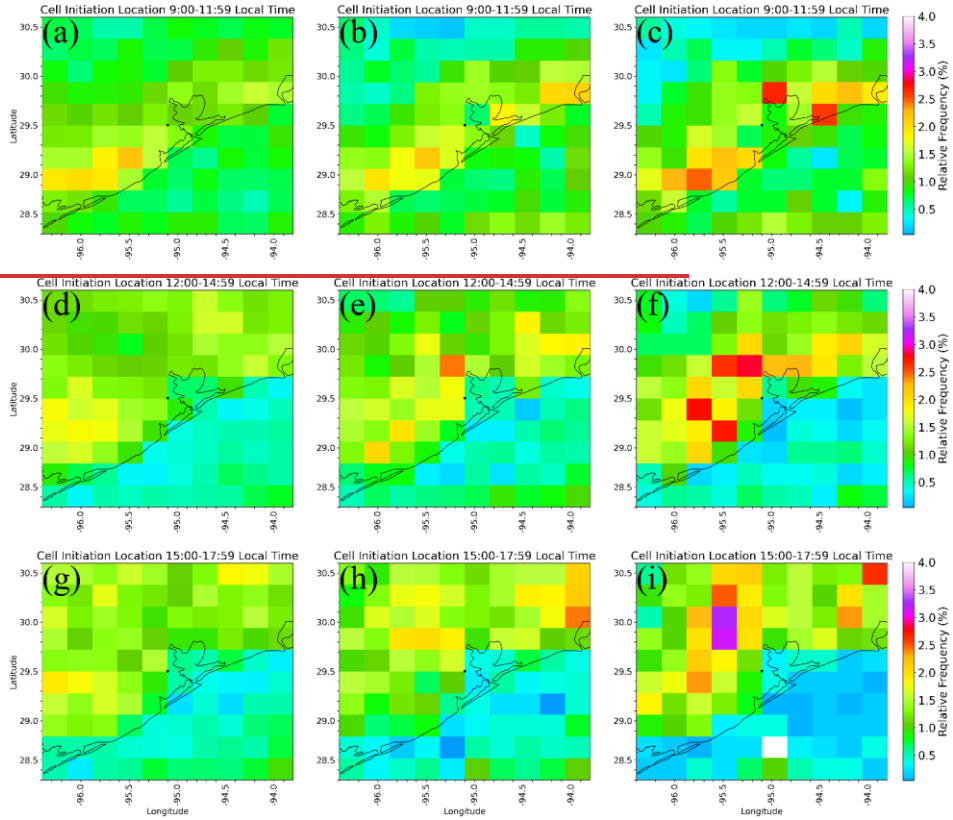
Cell Initiation Location 9:00-11:59 Local Time
(a)
Cell Initiation Location 9:00-11:59 Local Time
(b)
Cell Initiation Location 9:00-11:59 Local Time
(c)
Cell Initiation Location 12:00-14:59 Local Time
(d)
Cell Initiation Location 12:00-14:59 Local Time
(e)
Cell Initiation Location 12:00-14:59 Local Time
(f)
Cell Initiation Location 15:00-17:59 Local Time
(g)
Cell Initiation Location 15:00-17:59 Local Time
(h)
Cell Initiation Location 15:00-17:59 Local Time
(i)
Latitude
Longitude
Relative Frequency (%)
30.5
30.0
29.5
29.0
28.5
-96.0
-95.5
-95.0
-94.5
-94.0
4.0
3.5
3.0
2.5
2.0
1.5
1.0
0.5

~~Figure 6~~

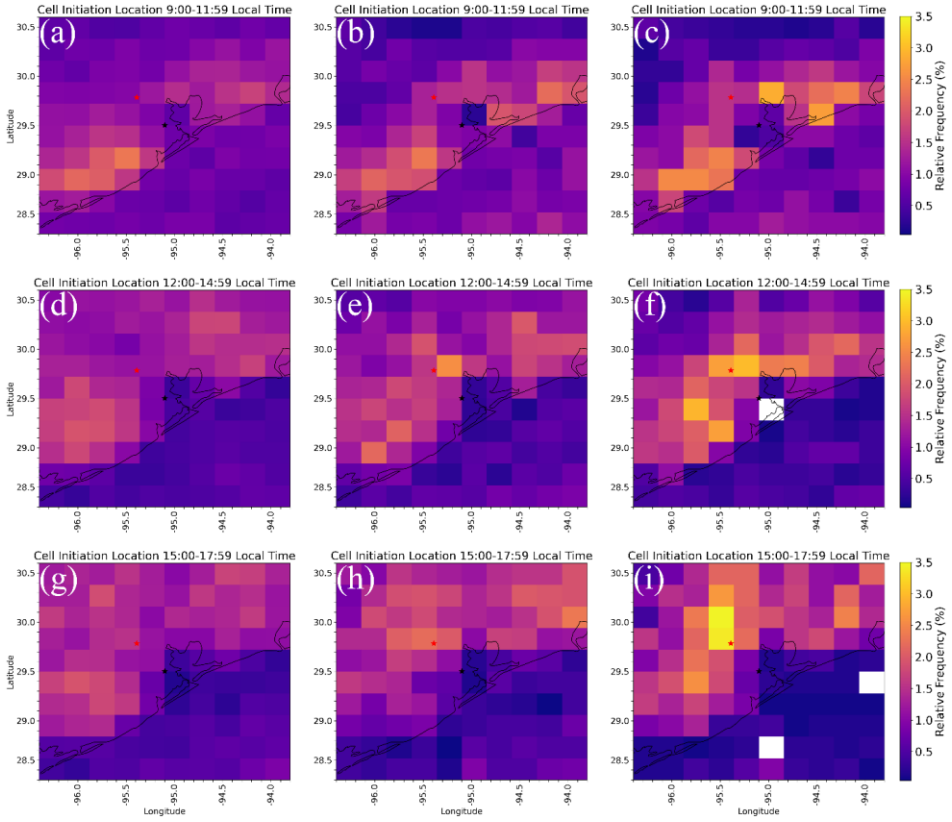

Figure 5: Maps showing the spatial distributions of initiation locations normalized by the number of cells that initiated during that period for the 3-hour periods 09:00 to 11:59 (a, b, c), 12:00 to 14:59 (d, e, f), and 15:00 to 17:59 (g, h, i), local time for shallow (a, d, g), modest deep (b, e, h), and vigorous deep (c, f, i) convection. The black (red) star in each plot denotes the location of KHGX (downtown Houston).

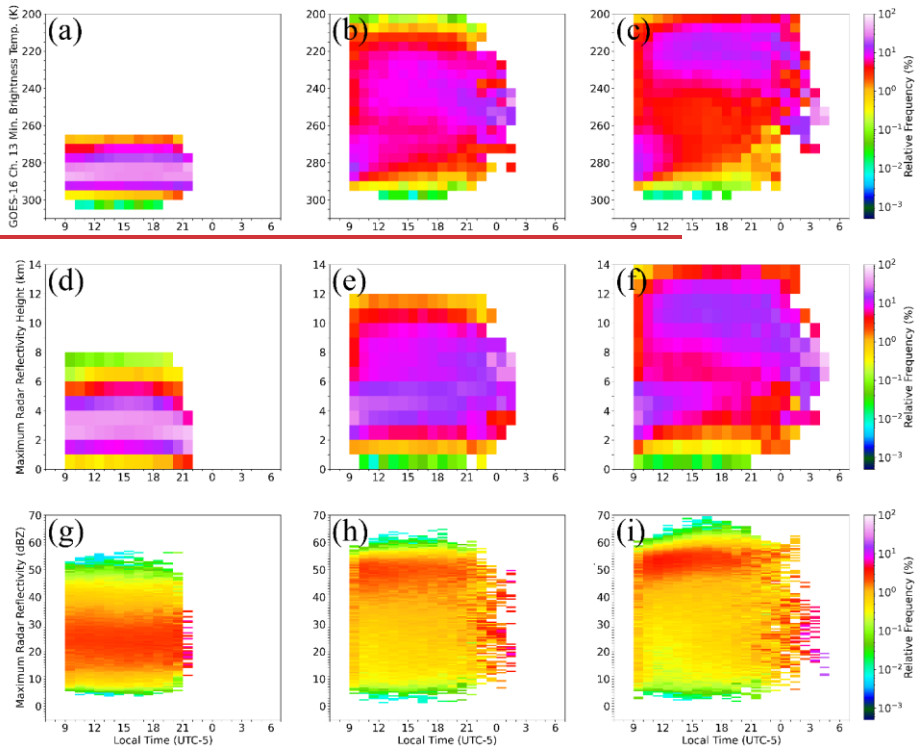
(a)
(b)
(c)
(d)
(e)
(f)
(g)
(h)
(i)
GOES-16 Ch. 13 Min. Brightness Temp. (K)
Maximum Radar Reflectivity Height (km)
Maximum Radar Reflectivity (dBZ)
Relative Frequency (%)
Local Time (UTC-5)

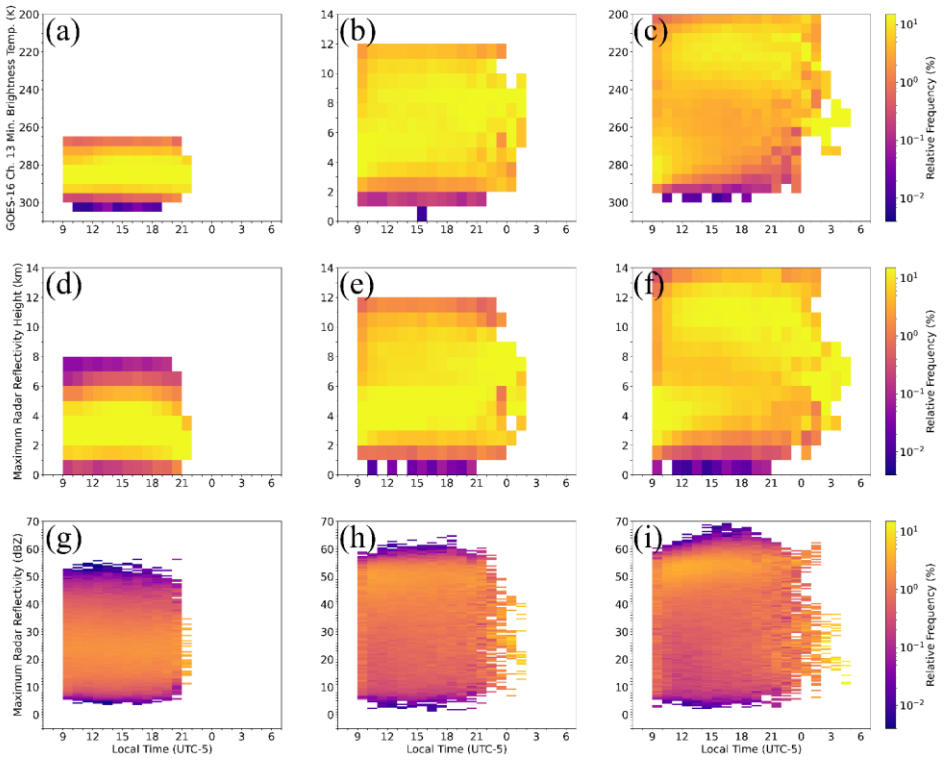

Figure ~~7~~6: The time bin normalized distributions of GOESBT (a, b, c), H_{dBZmax} (d, e, f), and dBZ_{max}(g, h, i) over the course of a day for all scans over the lifetimes of shallow (a, d, g), modest deep (b, e, h), and vigorous deep (c, f, i) convection.

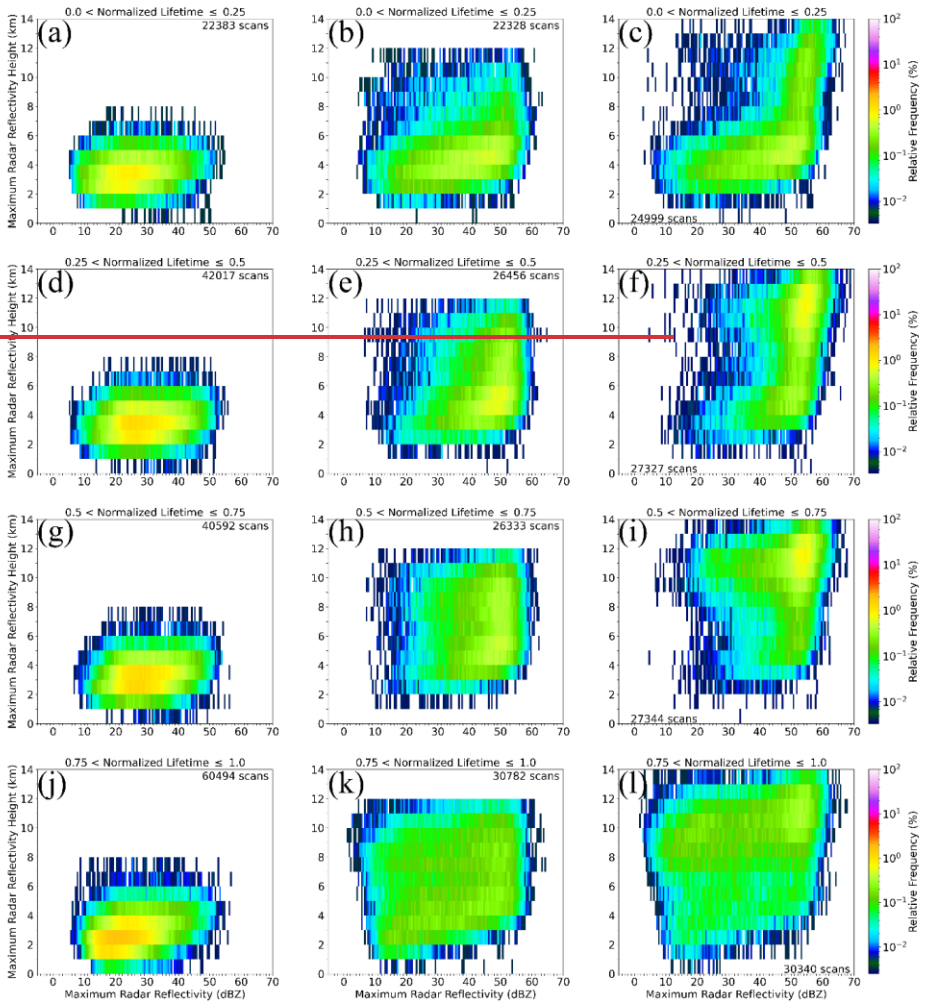
0.0 < Normalized Lifetime ≤ 0.25
(a)
22383 scans
(b)
22328 scans
(c)
24999 scans
0.25 < Normalized Lifetime ≤ 0.5
(d)
42017 scans
(e)
26456 scans
(f)
27327 scans
0.5 < Normalized Lifetime ≤ 0.75
(g)
40592 scans
(h)
26333 scans
(i)
27344 scans
0.75 < Normalized Lifetime ≤ 1.0
(j)
60494 scans
(k)
30782 scans
(l)
30340 scans
Maximum Radar Reflectivity Height (km)
Maximum Radar Reflectivity (dBZ)
Relative Frequency (%)

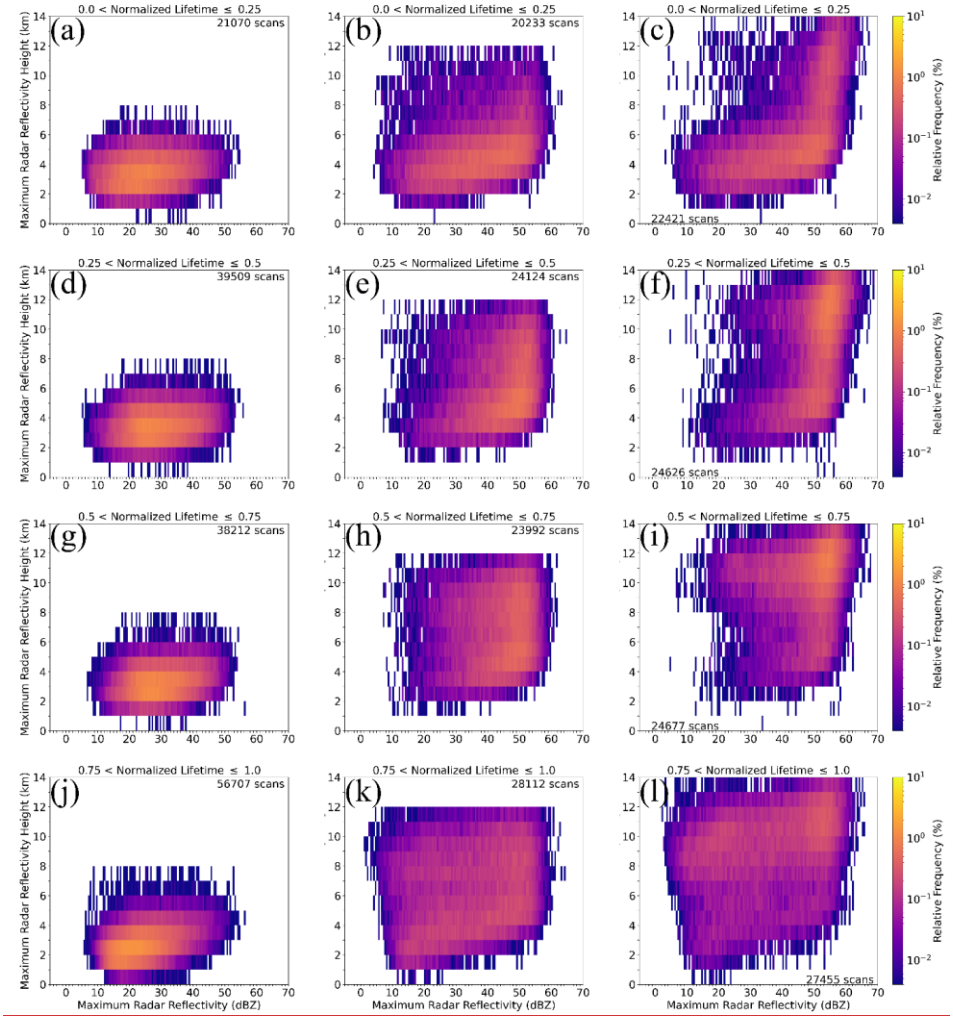

Figure ~~8~~7: The distributions normalized by the number of scans considered for each cell lifetime segment of dBZ_{max} versus H_{dBZmax} for the first 25% (a, b, c), the second 25% (b, e, f), the third 25% (g, h, i), and the final 25% of cell lifetimes (j, k, l) for shallow (a, d, g, j), modest deep (b, e, h, i), and vigorous deep (c, f, i, l) convection.

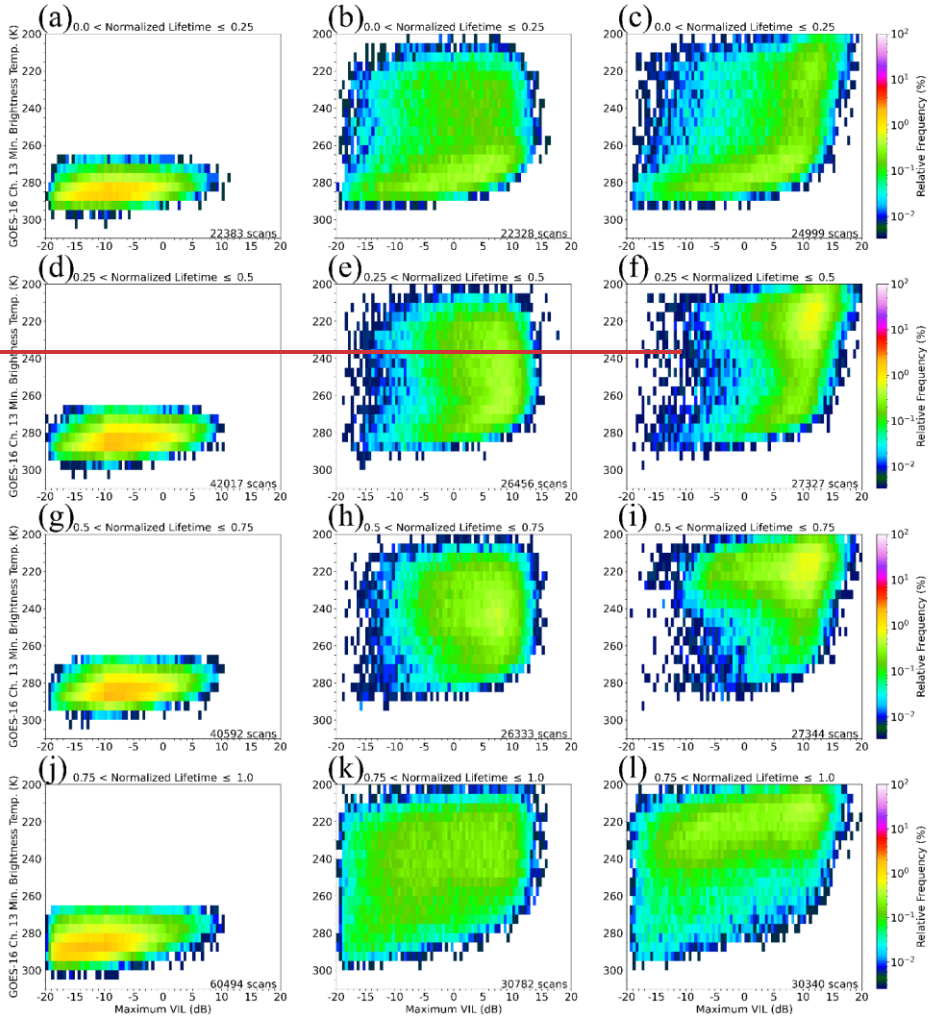
(a) 0.0 < Normalized Lifetime ≤ 0.25
22383 scans
(b) 0.0 < Normalized Lifetime ≤ 0.25
22328 scans
(c) 0.0 < Normalized Lifetime ≤ 0.25
24999 scans
(d) 0.25 < Normalized Lifetime ≤ 0.5
42017 scans
(e) 0.25 < Normalized Lifetime ≤ 0.5
26456 scans
(f) 0.25 < Normalized Lifetime ≤ 0.5
27327 scans
(g) 0.5 < Normalized Lifetime ≤ 0.75
40592 scans
(h) 0.5 < Normalized Lifetime ≤ 0.75
26333 scans
(i) 0.5 < Normalized Lifetime ≤ 0.75
27344 scans
(j) 0.75 < Normalized Lifetime ≤ 1.0
60494 scans
(k) 0.75 < Normalized Lifetime ≤ 1.0
30782 scans
(l) 0.75 < Normalized Lifetime ≤ 1.0
30340 scans
GOES-16 Ch. 13 Min. Brightness Temp. (K)
Maximum VIL (dB)
Relative Frequency (%)

800

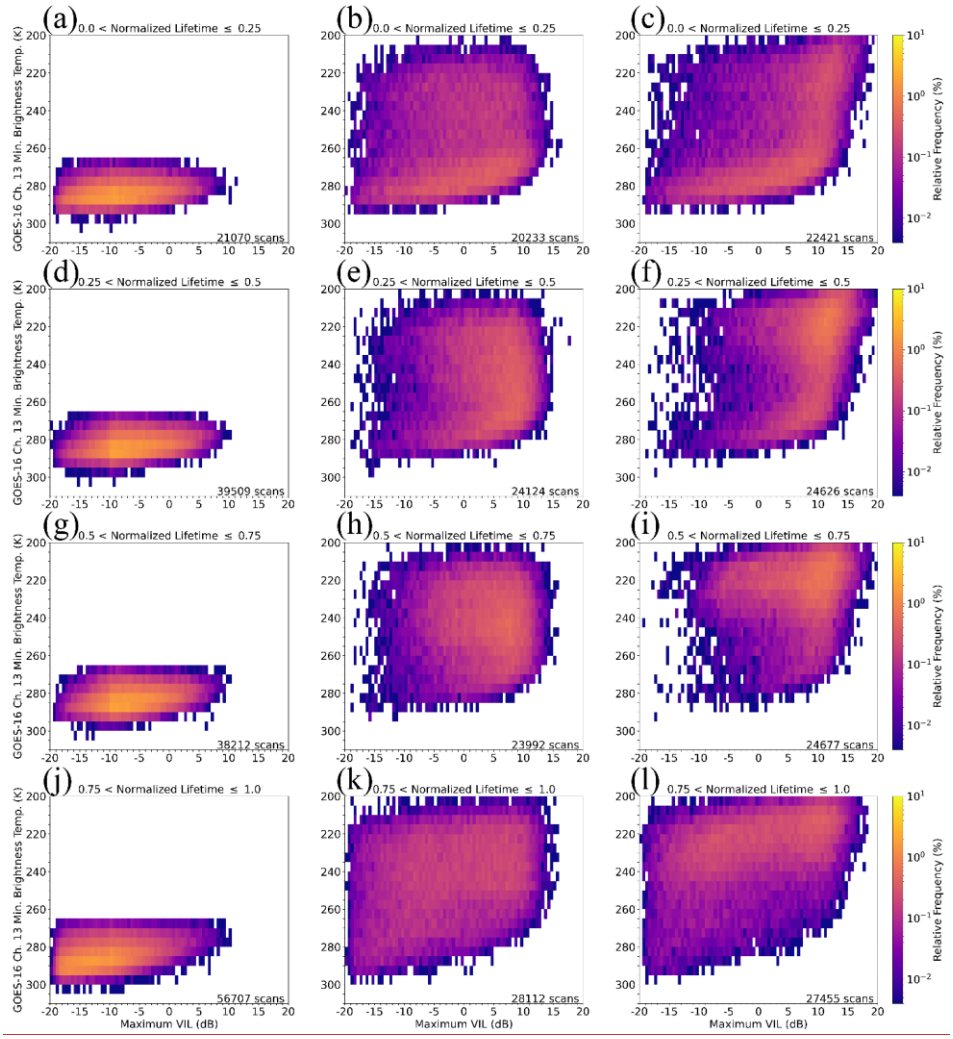

Figure ~~Figure 9: As in Fig.~~ 8: As in Fig. 7, but for maximum VIL versus GOESBT.

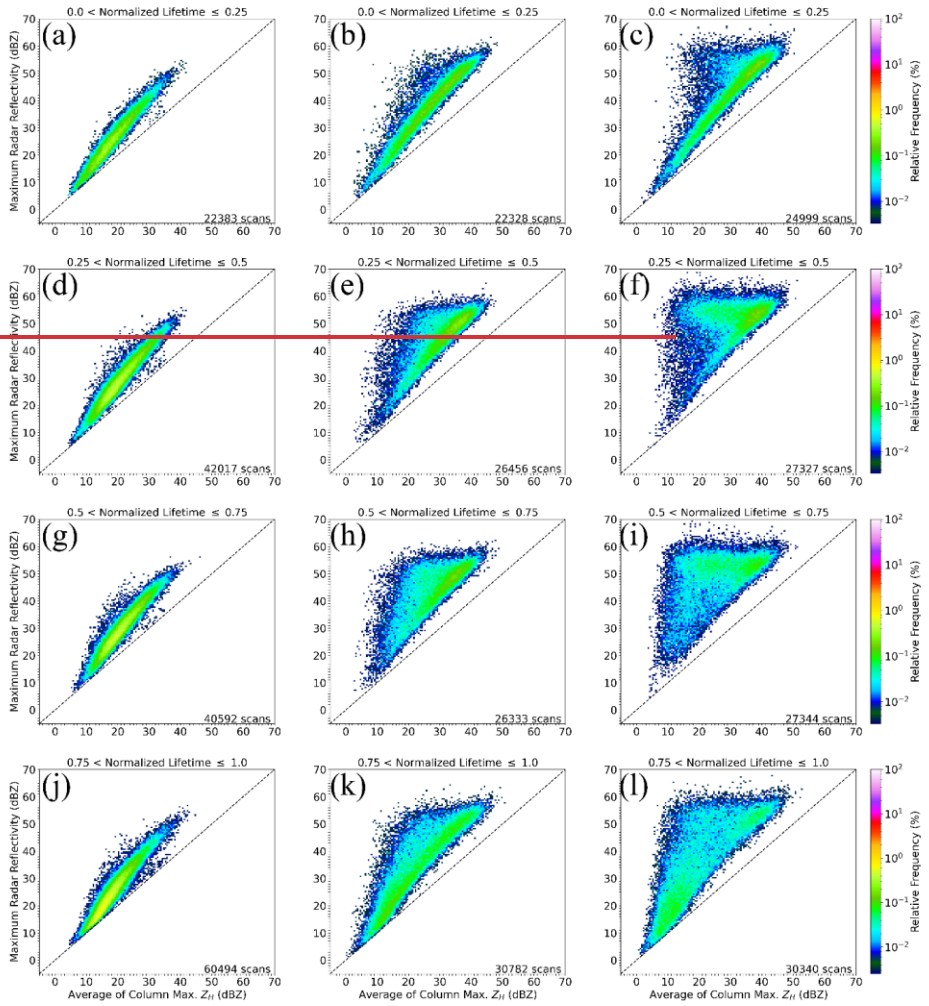
0.0 < Normalized Lifetime ≤ 0.25
(a)
22383 scans
(b)
22328 scans
(c)
24999 scans
0.25 < Normalized Lifetime ≤ 0.5
(d)
42017 scans
(e)
26456 scans
(f)
27327 scans
0.5 < Normalized Lifetime ≤ 0.75
(g)
40592 scans
(h)
26333 scans
(i)
27344 scans
0.75 < Normalized Lifetime ≤ 1.0
(j)
60494 scans
(k)
30782 scans
(l)
30340 scans
Maximum Radar Reflectivity (dBZ)
Average of Column Max. Z_H (dBZ)
Relative Frequency (%)

~~Figure 10: As in Fig. 8~~

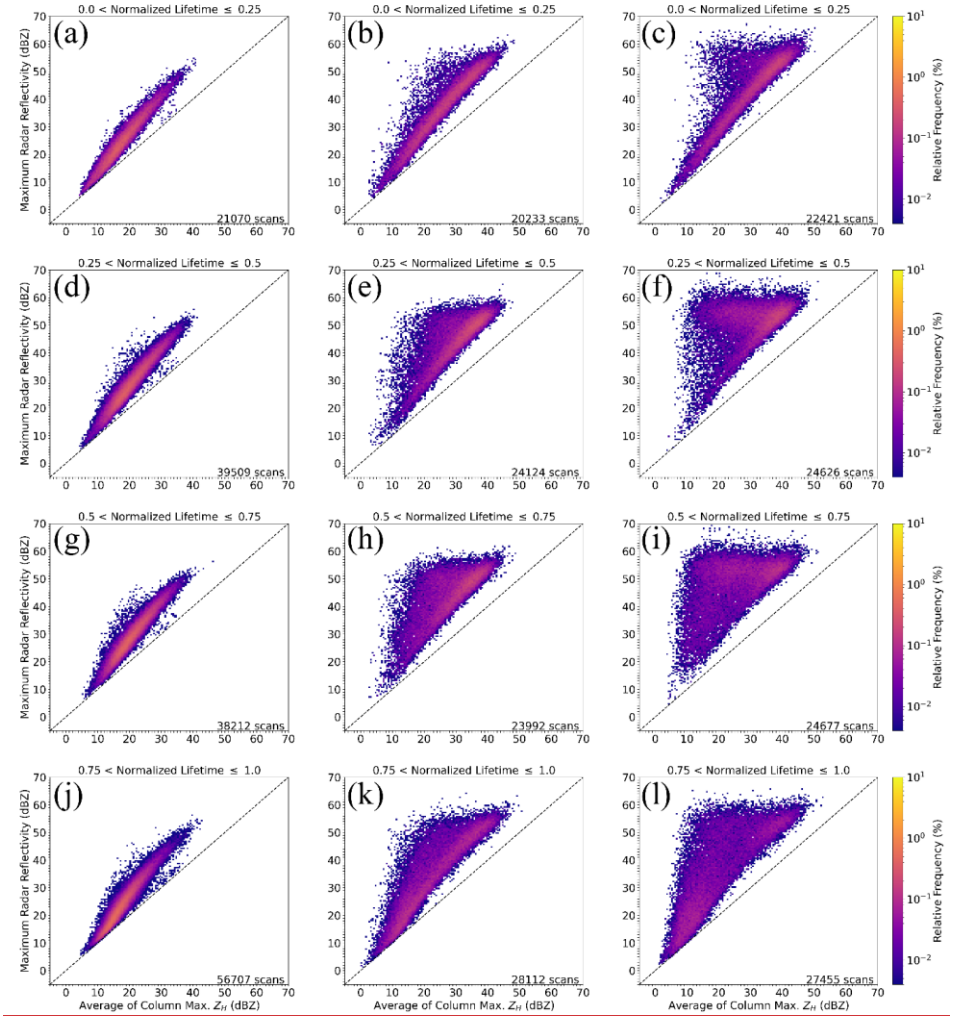

Figure 9: As in Fig. 7, but for dBZ_{avg} versus dBZ_{max}. The dashed line shows the one-to-one value of dBZ_{avg} and dBZ_{max}.

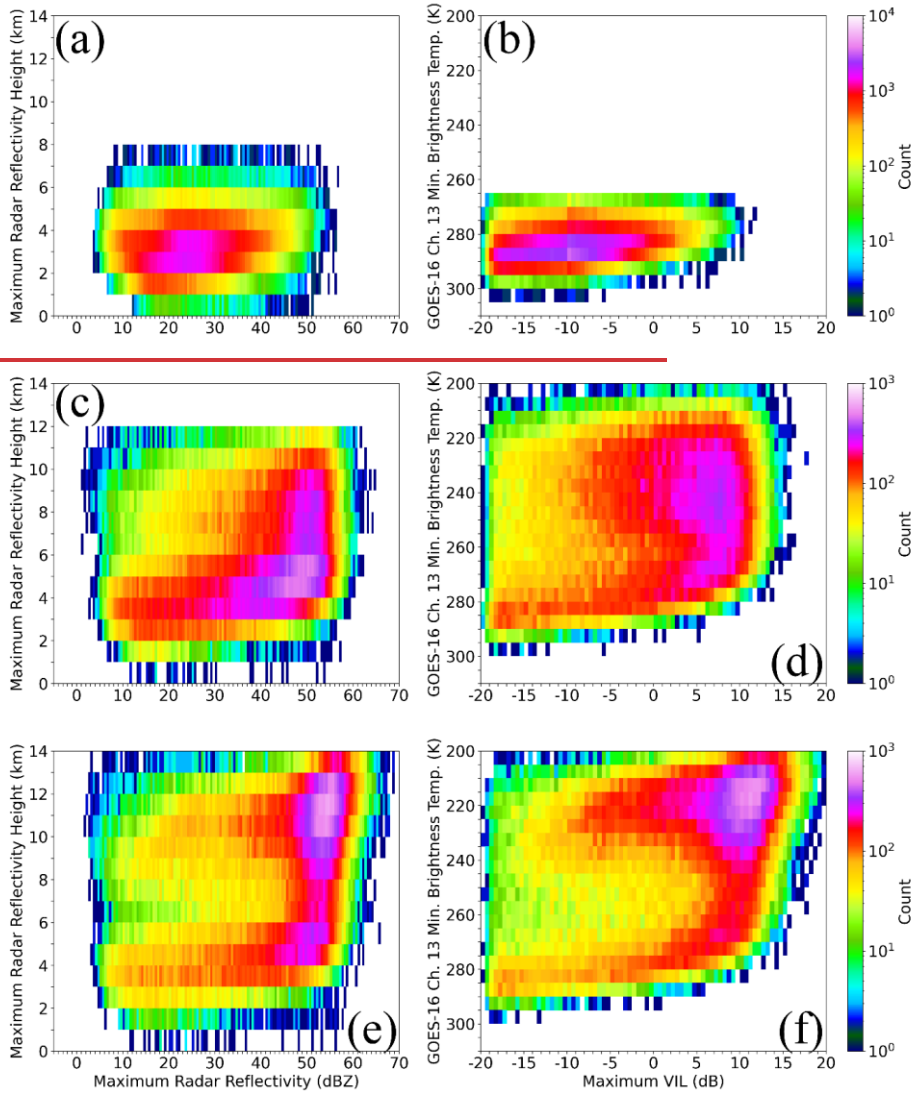

Figure 11: The aggregates of all radar scans for the entire lifetimes of all cell types for dBZ_{max} versus H_{dBZmax} (a, c, e) and maximum VIL versus GOESBT (b, d, f) for shallow (a, b), modest deep (c, d), and vigorous deep (e, f) convective cells.

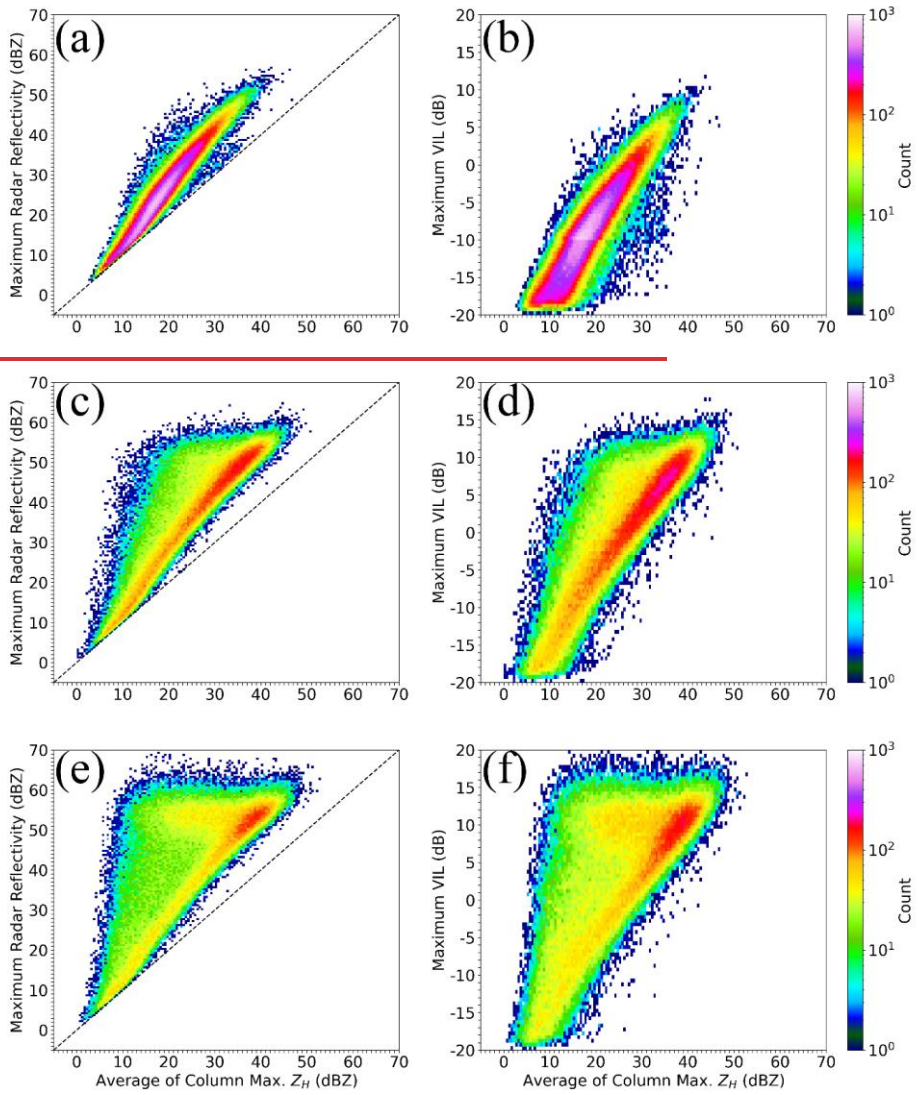

Figure 12: As in Fig. 11, but for the dBZ_{avg} versus dBZ_{max} (a, c, e) and dBZ_{avg} versus maximum VIL (b, d, f). The dashed line in (a, c, e) shows the one-to-one value of dBZ_{avg} and dBZ_{max}.

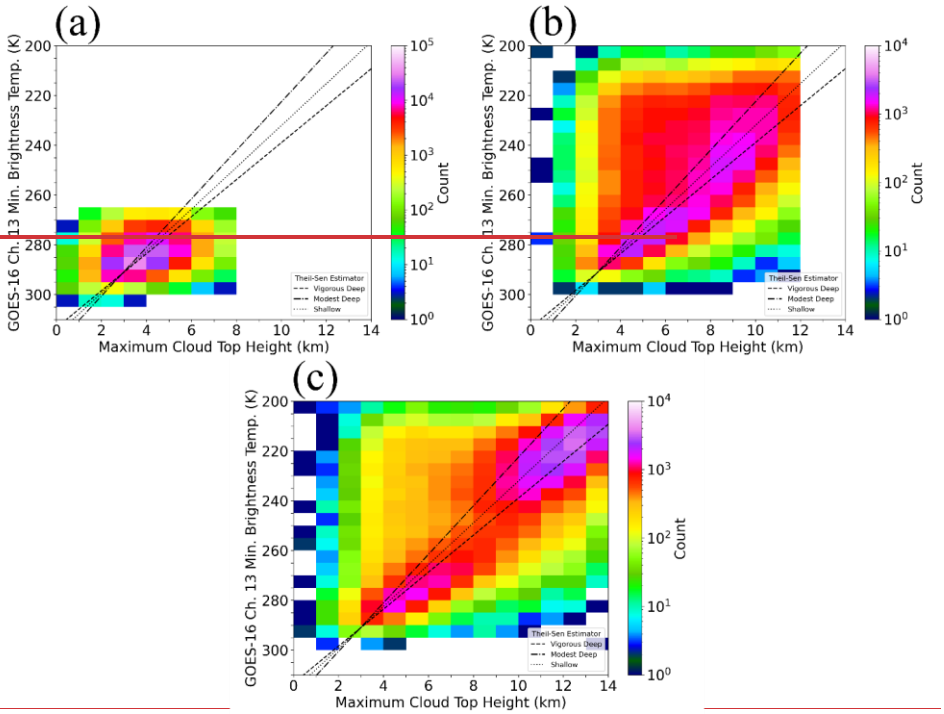

Figure 13: The distributions of CTH versus GOESBT for all scans of shallow (a), modest deep (b), and vigorous deep (c) convection. The lines denote the Theil-Sen estimator regression performed on shallow (dotted), modest deep (dot-dash), and vigorous deep (dashed) convection.

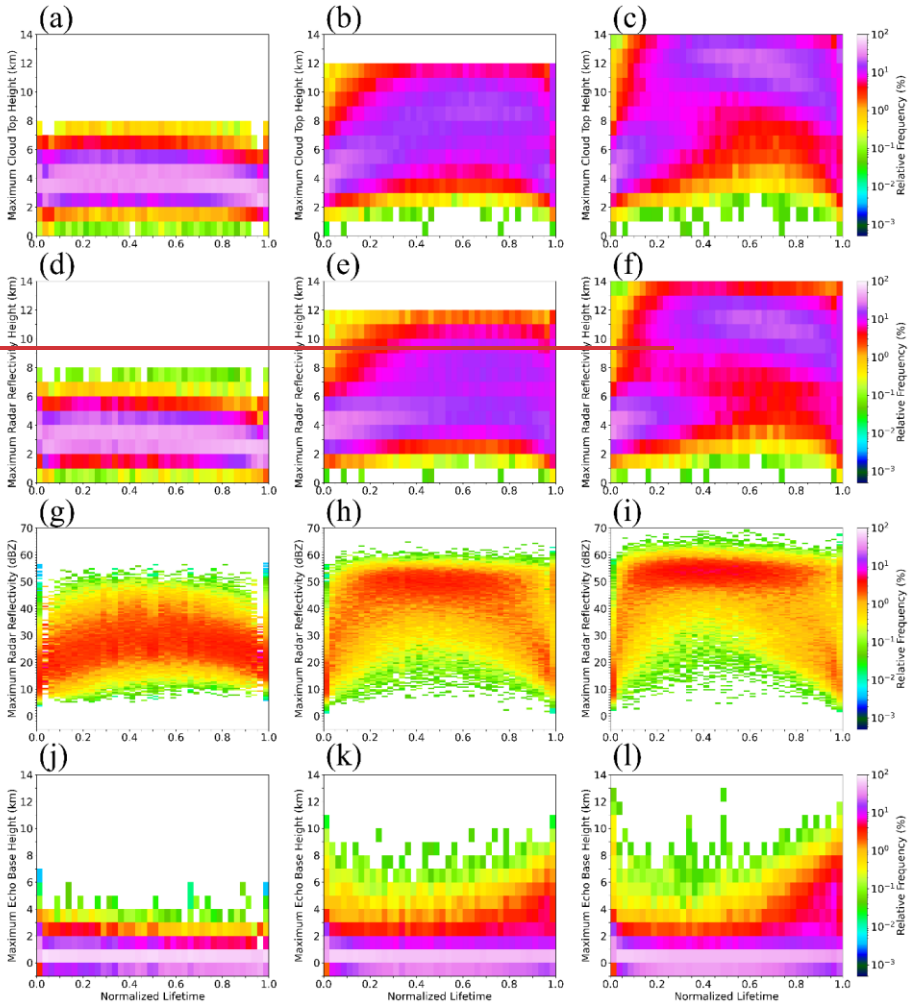
(a)
(b)
(c)
(d)
(e)
(f)
(g)
(h)
(i)
(j)
(k)
(l)
Maximum Cloud Top Height (km)
Maximum Radar Reflectivity Height (km)
Maximum Radar Reflectivity (dBZ)
Maximum Echo Base Height (km)
Normalized Lifetime
Relative Frequency (%)

Figure 14:

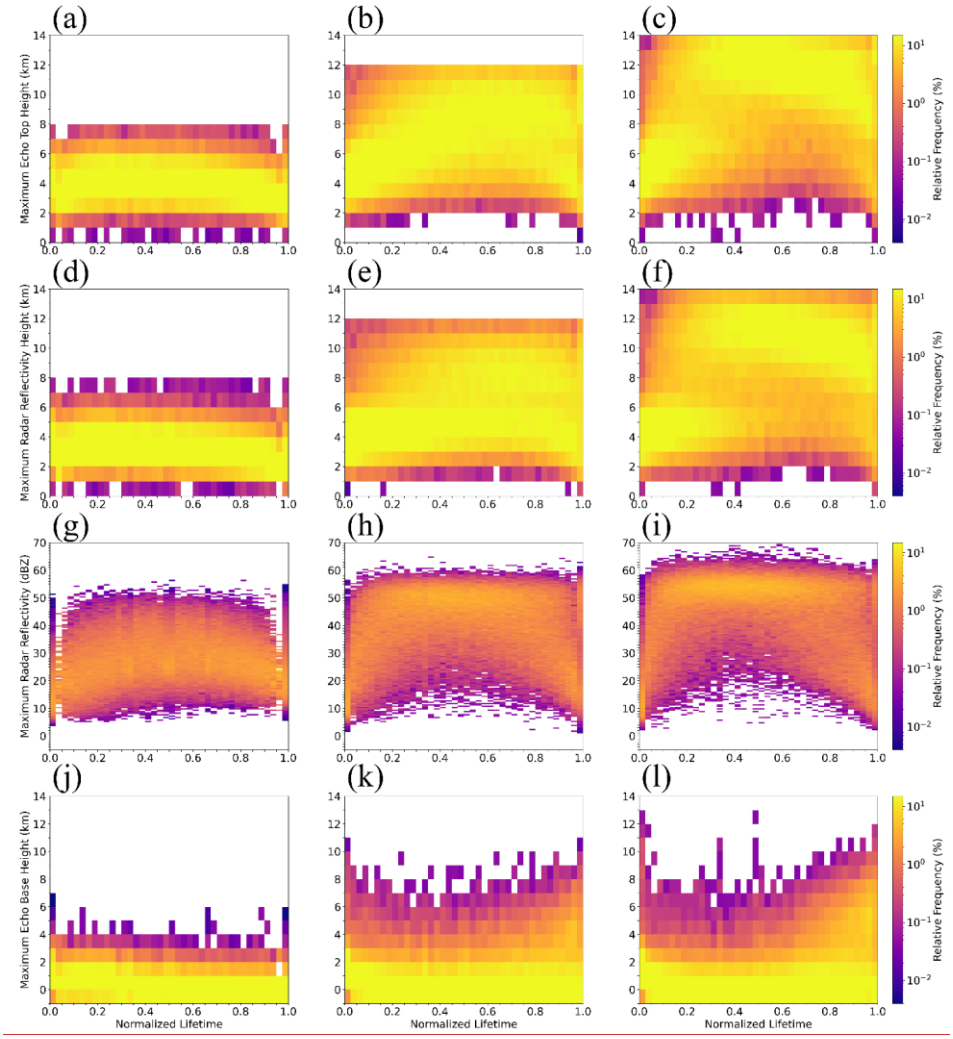

Figure 10: The bin normalized distributions for normalized lifetime evolutions of ~~CTH~~ETH (a, b, c), H_{dBZmax} (d, e, f), dBZ_{max} (g, h, i), and H_{EBase} (j, k, l) for shallow (a, d, g, j), modest deep (b, e, h, k), and vigorous deep (c, f, i, l) convection.

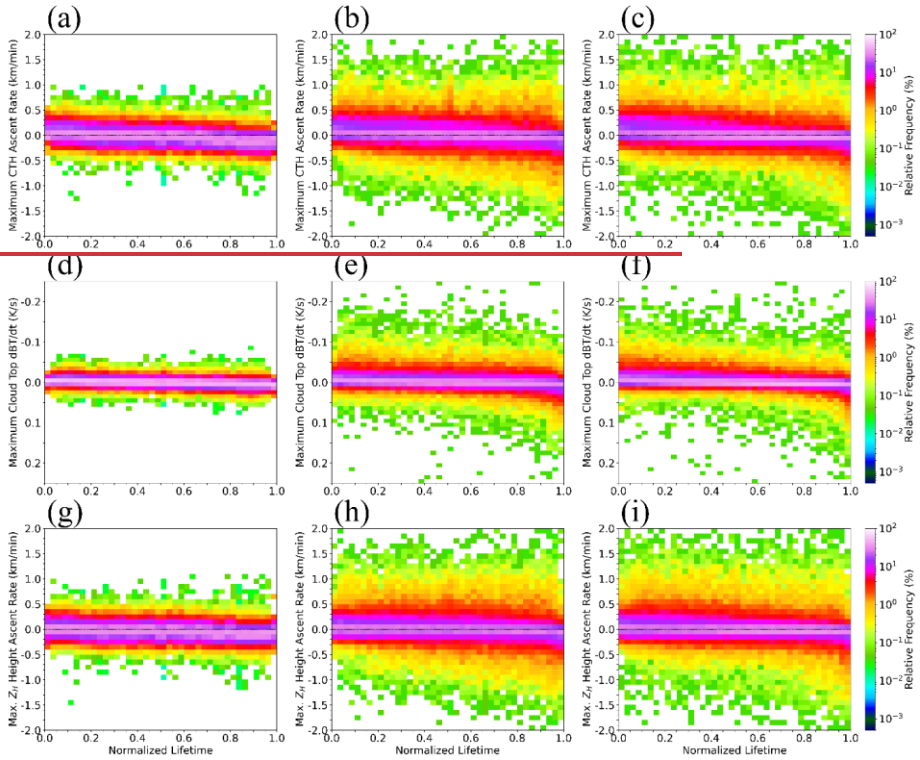
(a)
(b)
(c)
(d)
(e)
(f)
(g)
(h)
(i)
Maximum CTH Ascent Rate (km/min)
Maximum Cloud Top dBT/dt (K/s)
Max. Z_H Height Ascent Rate (km/min)
Normalized Lifetime
Relative Frequency (%)

825

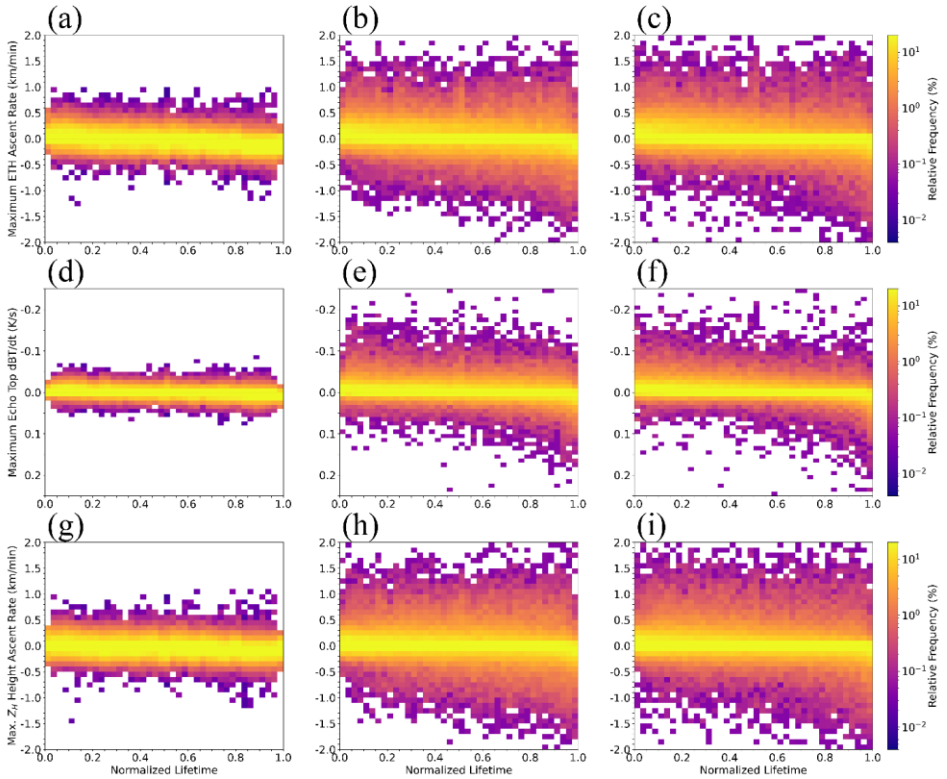

Figure ~~15~~11: The bin normalized ~~CTH~~ETH (a, b, c), GOESBT (d, e, f), and H_{dBZmax} (g, h, i) based ascent rates for shallow (a, d, g), modest deep (b, e, h), and vigorous deep (c, f, i) convection. The dashed line denotes the zero-change line.

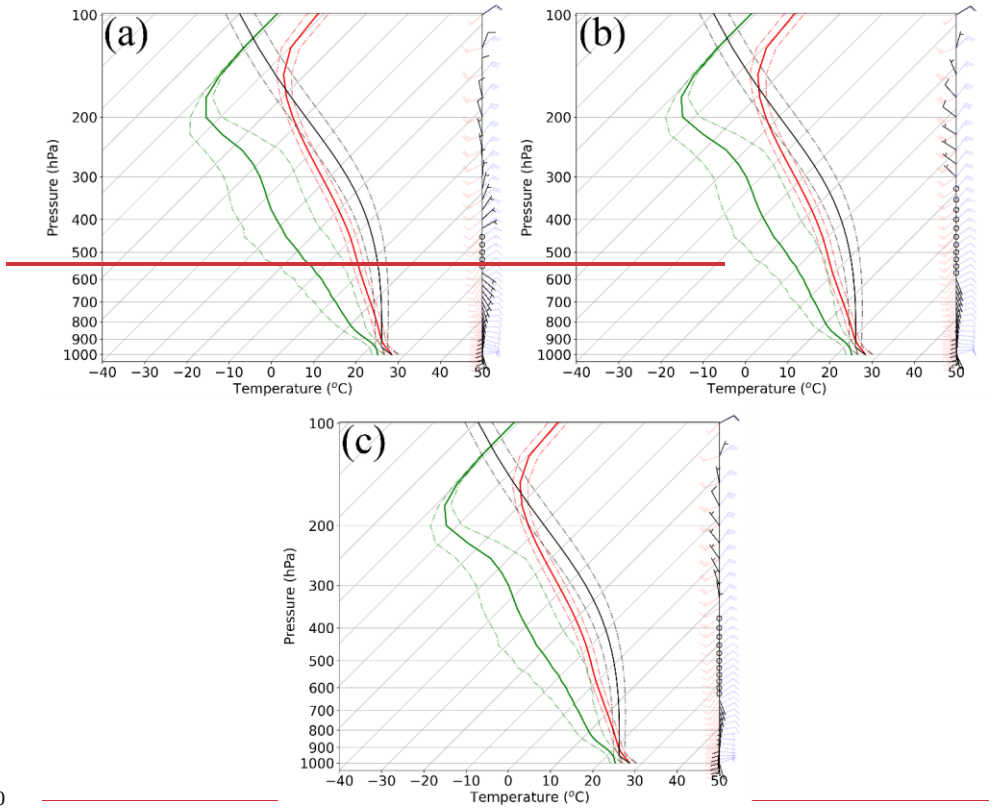

Figure 16: Composite HRRR soundings for the initiation location of shallow (a), modest deep (b), and vigorous deep (c) convection. The red, green, and black solid (dot-dashed) lines represent the mean (± one standard deviation) of temperature, dew point, and parcel path respectively. Black, red, and blue wind barbs represent the mean, plus one, and minus one standard deviation in knots.

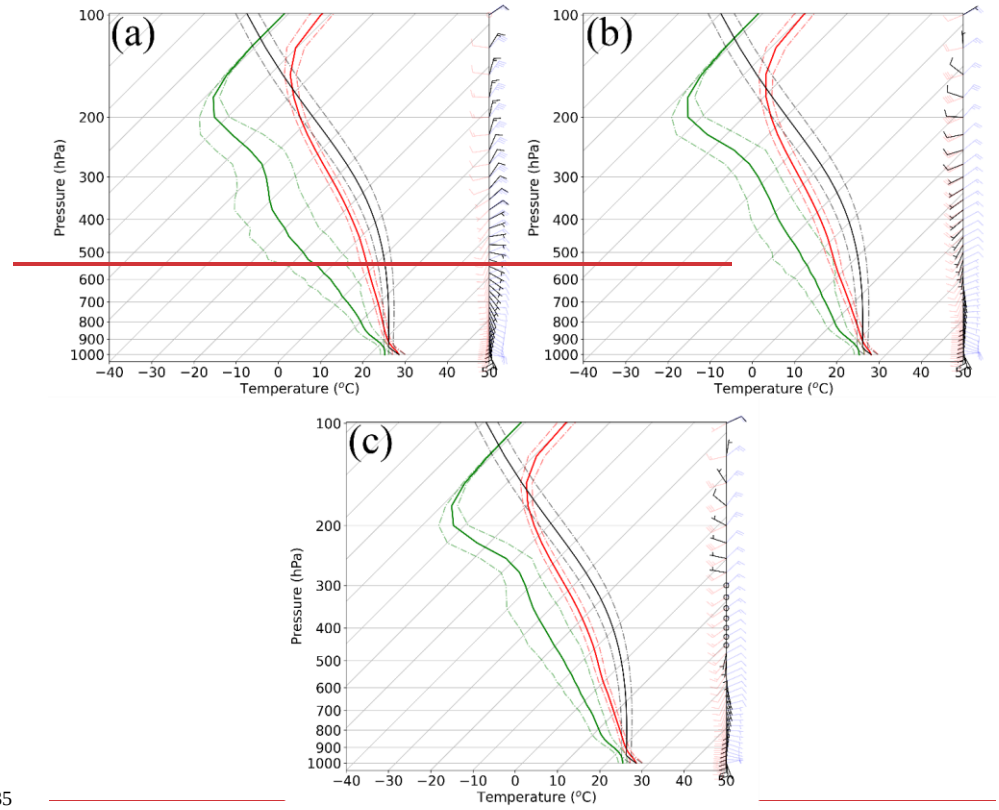

Figure 17: As in Fig. 16, but for days where the 95th percentile of daily cell count was surpassed for each case type.

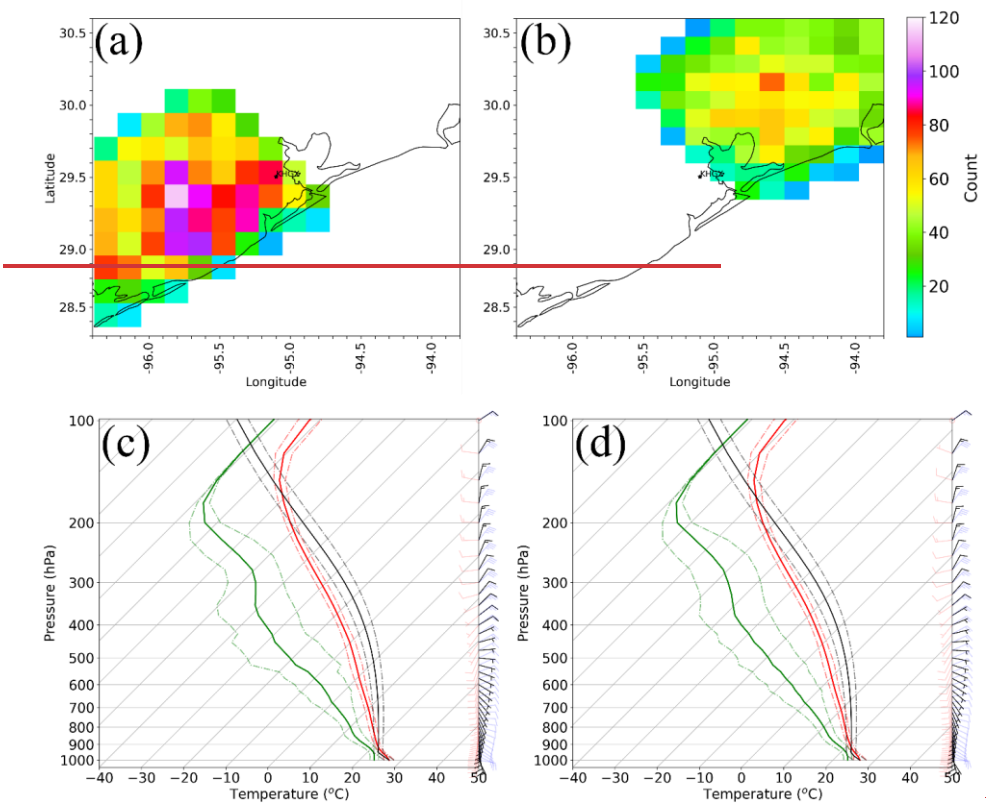

Figure 18: Subsets of the initiation locations for shallow convection on days where the 95th percentile of daily shallow convective cell counts was surpassed (a, b) and the composite soundings for cells that initiated to the southwest (c) and northeast (d) of Houston. Sounding plot depictions are as in Fig. 16.

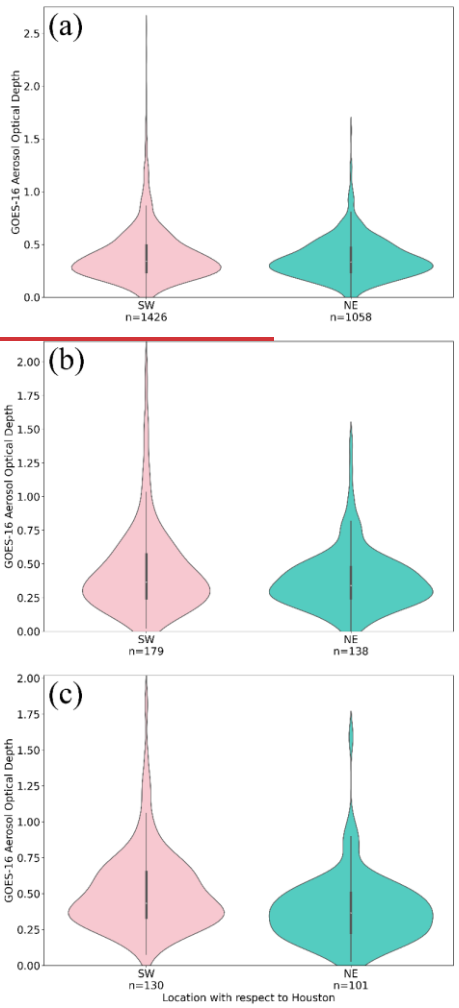
(a)
GOES-16 Aerosol Optical Depth
SW
n=1426
NE
n=1058
(b)
GOES-16 Aerosol Optical Depth
SW
n=179
NE
n=138
(c)
GOES-16 Aerosol Optical Depth
SW
n=130
NE
n=101
Location with respect to Houston

~~Figure 19~~

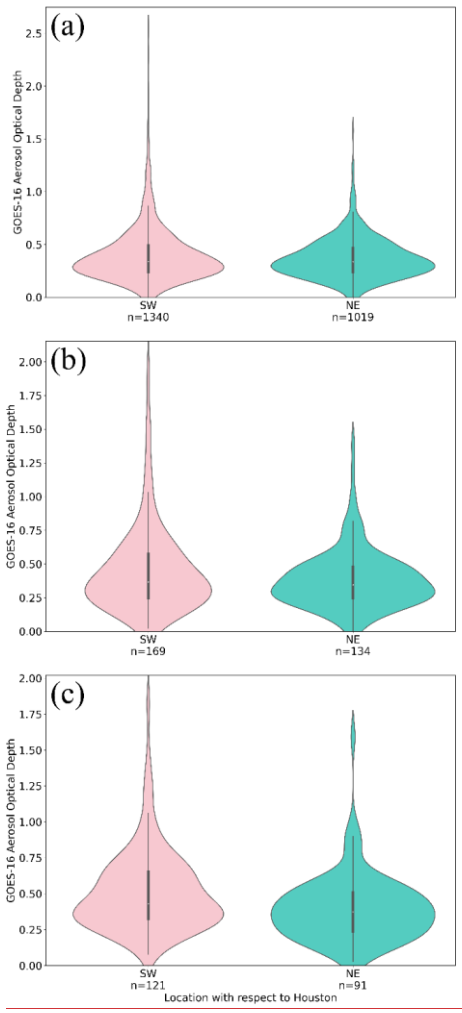

Figure 12: Violin plots depicting the distributions of the average of the 30-minute AOD values for the period prior to cell initiation to the southwest (red; same region as Fig. 18a) and northeast (blue; same region as Fig. 18b) of Houston for (a) shallow, (b) modest deep, and (c) vigorous deep convective cells. The number n under each violin plot corresponds to the number of cells considered for each distribution.

Appendix Tables and Figures

Shallow Convection				
	-5%		+5%	
	n	% change	n	% change
All Thresholds Simultaneously	44560416894456041689	15.858215.8582	19074178551907417855	-50.414050.4140
Lifetime Max. Area	37435350183743535018	-2.68722.6872	39363368513936336851	2.33382.3338
Lifetime Min. GOESBT	44982420384498242038	16.947916.9479	19620183691962018369	-48.999748.9997
Lifetime Max. CRatioERatio	38518360473851836047	0.14	38376359113837635911	-0.232400.2324
Lifetime Max. CTHETH	38285358453828535845	-0.474200.4742	38570360903857036090	0.272600.2726
Lifetime Max. VIL	39389369063938936906	2.405302.4053	37465350553746535055	-2.606102.6061
Modest Deep Convection				
	-5%		+5%	
	n	% change	n	% change
All Thresholds Simultaneously	541649935416493	-36.393708.0736.3937.08	108431016810843101681	27.352814.0527.3528.14
Lifetime Min. GOESBT	621457746214577	-27.012327.0123	1055298711055298710	23.942440.0023.9424.40
Lifetime Max. CRatioERatio	853579568535795	0.252600.2526	848479068484790	-0.353700.3537
Lifetime Max. CTHETH (Lower Bound)	92148566921485	8.227.958.227.95	782973127829731	-8.057.858.057.85
Lifetime Max. CTHETH (Upper Bound)	702965267029652	-17.447617.4476	991792479917924	16.485316.4853
Lifetime Max. VIL	857079908570799	0.666900.6669	845178798451787	-0.747100.7471
Vigorous Deep Convection				
	-5%		+5%	
	n	% change	n	% change
All Thresholds Simultaneously	636159336361593	21.468521.4685	387935993879359	-25.932608.0025.9326.08
Lifetime Min. GOESBT	504246845042468	-3.728003.7280	534949755349497	2.141802.1418
Lifetime Max. CRatioERatio	524148735241487	0.08	523148635231486	-0.111200.1112
Lifetime Max. CTHETH	672262786722627	28.369428.3694	383435573834355	-26.799526.7995
Lifetime Max. VIL	524548775245487	0.151600.1516	522948625229486	-0.151400.1514

Table A1: A table showing the sensitivity of cell selection based on ±5% adjustments of a given variable. The number n represents the number of cells selected after the threshold adjustments were applied. Values for the percent change in the number of cells selected colored in green, yellow, and red denote cells with percent changes ≤ ±10%, ≤ ±20% and > ±20% respectively.

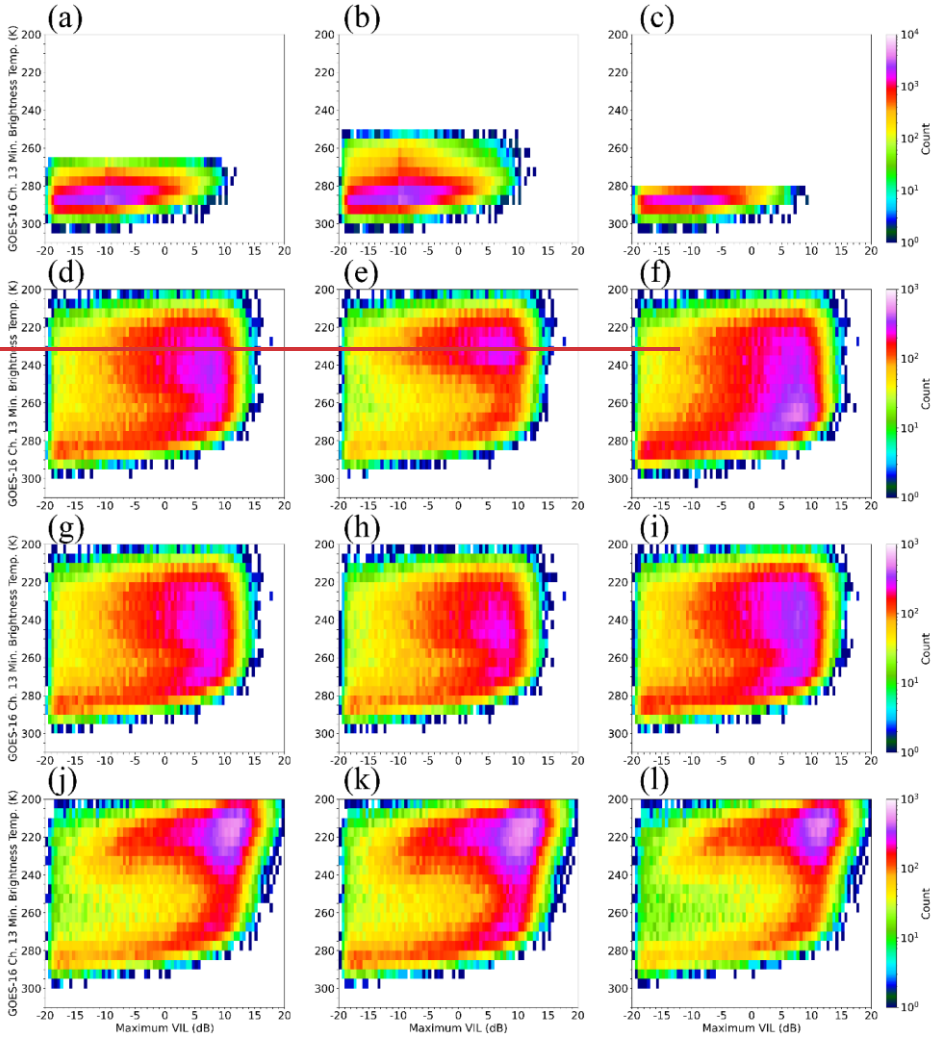
(a)
(b)
(c)
(d)
(e)
(f)
(g)
(h)
(i)
(j)
(k)
(l)
GOES-16 Ch. 13 Min. Brightness Temp. (K)
Maximum VIL (dB)
Count

855

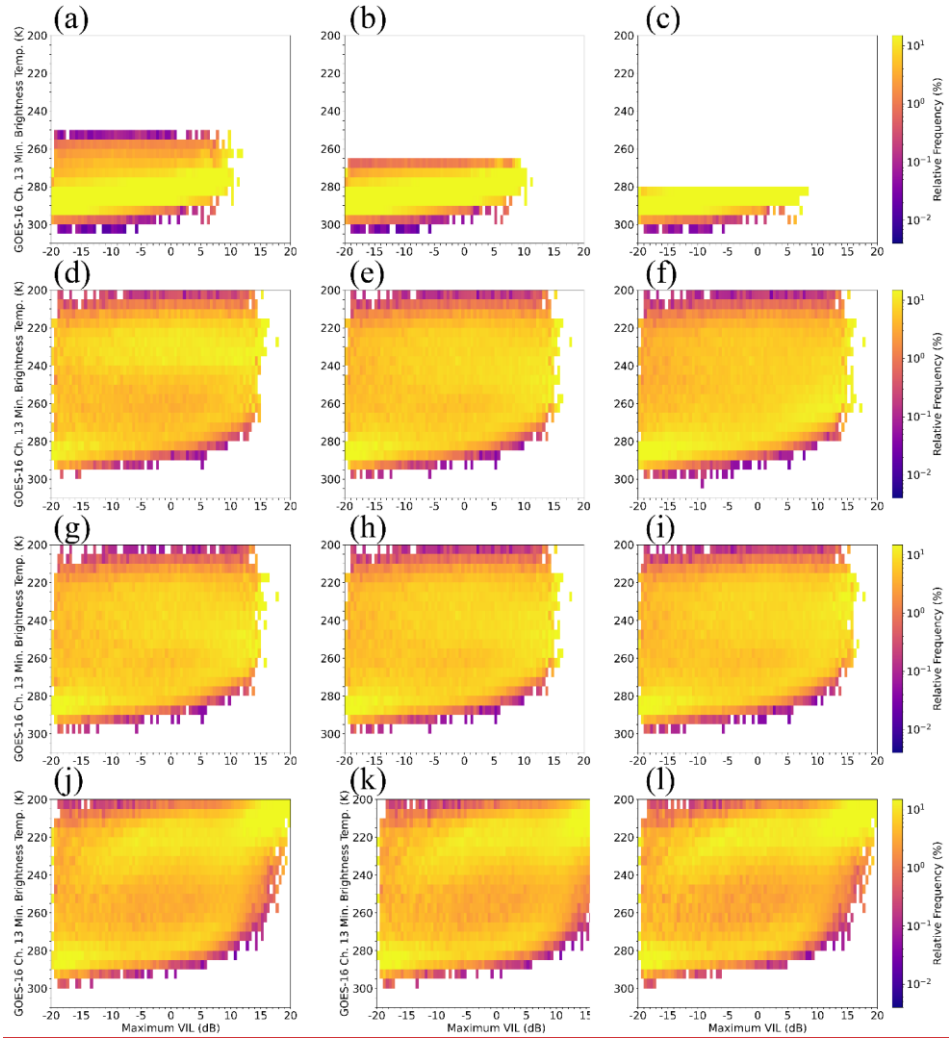

Figure A1: The lifetime distributions of GOESBT versus maximum VIL to illustrate threshold sensitivity for the most highly sensitive variables shown in table A1. The baseline (no change) distributions are shown in (a, d, g, j), 5% decrease is shown in (b, e, h, k) and 5% increase is shown in (c, f, i, l) for shallow convection GOESBT sensitivity (a,b,c), modest deep convection GOESBT sensitivity (d, e, f), ~~vigorous~~modest deep convection ~~CRatio~~upper bound ERatio sensitivity (g, h, i) and vigorous deep convection ~~CTH~~ETH sensitivity (j, k, l).